Degradation of P3HT:PCBM-based Conjugated Polymer Solar Cells

by

Shabnam Shambayati

B.A.Sc., The University of British Columbia, 2008

A THESIS SUBMITTED IN PARTIAL FULFILLMENT OF
THE REQUIREMENTS FOR THE DEGREE OF

MASTER OF APPLIED SCIENCE

in

The Faculty of Graduate Studies

(Electrical & Computer Engineering)

THE UNIVERSITY OF BRITISH COLUMBIA

(Vancouver)

August 2011

Abstract

This work examines the effect of regioregularity (RR) and zinc oxide (ZnO) nanoparticle doping on the degradation of poly(3-hexylthiophene) (P3HT):6,6-phenyl C_{61}-butyric acid methyl ester (PCBM) organic solar cells. This is done through application of semi-compact models that relate experimentally measured transport characteristics to structural properties. In this way, the contribution of regioregularity and ZnO nanoparticles to the change in structural properties can be quantified. These models allow interpretation of experimental data and insight into the underlying degradation mechanisms. In this thesis, the mobility edge model is used, and corresponding parameters such as effective electron and hole mobilities are extracted and compared. These results show that studying electron transport plays a critical role in understanding the degradation of P3HT:PCBM solar cells.

Examination of regioregular devices reveals that the drop in effective electron mobility with annealing for the high RR devices is greater than that of the low RR ones. This is attributed to the greater tendency for crystallization-driven phase segregation in blends of 98% RR P3HT and PCBM. In hybrid polymer-ZnO devices, effective electron mobility improves with the addition of an optimal concentration of ZnO. The decline in electron effective mobilities with annealing is smaller for the devices containing ZnO in comparison to devices without ZnO. Studying the morphology of these devices shows that the phase segregation is identical for devices with and without ZnO.

Preface

Chapters 4 and 5 are based on work in collaboration with Dr. Steven Holdcroft's group at the Simon Fraser University department of chemistry. I have performed all of the experiments, generated and prepared the figures, and written the first draft of the thesis. I performed all of the analysis with input from Dr. Peyman Servati. I am responsible for the final version of this thesis, which incorporates suggestions from Dr. Peyman Servati and Dr. Bobak Gholamkhass. The transmission electron microscopy pictures in Chapter 5 were taken by Dr. Bobak Gholamkhass. Zinc oxide was prepared by Nima Mohseni Kiasari at the UBC Flexible Electronics and Energy Lab. The results of Chapter 4 have been previously published by Ebadian et al. ("Effects of annealing and degradation on regioregular polythiophene-based bulk heterojunction organic photovoltaic devices," Solar Energy Materials & Solar Cells 94 (2010) pp. 2258-2264), and Shambayati et al. ("Modeling the effect of annealing and regioregularity on electron and hole transport characteristics of bulk heterojunction organic photovoltaic devices," MRS Proceedings 1270 (2010) p. HH14-56).

Table of Contents

Appendices

List of Tables

List of Figures

Acknowledgements

I would like to thank Dr. Servati for offering me the opportunity of working at the Flexible Electronics and Energy Lab; Dr. Pulfrey for teaching me how to be curious again; and Dr. Madden for kindly guiding me. Thank you Dr. Gholamkhass for being the most patient and knowledgable mentor I could ask for, and Dr. Steven Holdcroft for allowing me welcome access to the Holdcroft Lab. Thank you Drs. Dunbar and Stull for your support.

Thank you Ali Kashefian for knowing all of everything, and your graceful conversations; Nima Mohseni for your humor and friendship; and Dan Oh for helping me through the long days and weeks with patience and pasta salad, and pretending to be interested in my obsessive talk about work.

I would also like to thank my parents for more reasons than I can count, but especially my mother for her million sweetnesses, and my father for his intricate wisdom.

For PLT,
who understands things.

Chapter 1

Introduction

1.1 Why Solar Cells?

In recent years, energy security has become a source of major concern. International and geopolitical conflicts, reports of peaking resources, evidence of environmental impacts of conventional energy production, rapid increase in global energy demand, and the pace of growth in developing countries have contributed to this concern [2]. One proposed solution to the problems of pollution, climate change, and energy insecurity has been large-scale conversion to clean, perpetual, and reliable energy such as wind, water, and solar energy systems [3–6]. Over the past decade, a number of politically unaffiliated, peer-reviewed studies have proposed that large-scale renewable energy plans to replace conventional energy production may be feasible. Fthenakis et al. [5] have analyzed the technical, geographical, and economic feasibility for solar energy to supply the energy needs of the U.S. and concluded that "it is clearly feasible to replace the present fossil fuel energy infrastructure in the U.S. with solar power and other renewables". Jacobson [6] evaluated several long-term energy systems according to environmental and other criteria, and reported that all new energy could be supplied by the combination of water, wind and solar by 2030 and all existing energy could be converted to these sources by 2050. These reports highlight the important role of solar technologies in moving towards a feasibly cleaner future.

In 2009, the world production of photovoltaic modules surpassed 1100GWh, of which more than the 50% was produced in Europe [7]. The future of solar cell is less bright in Canada: the 2007 report published by the National Energy Board [2] has concluded that even though the energy demand in Canada will continue to grow for the next 30 years, fossil fuel energy will

continue to be the dominant source of supply, although non-conventional and non-fossil fuel supplies will begin to play a larger role. The National Energy Board report concludes that for photovoltaics to become more prominent in Canada, better technology at lower cost is required, and proposes that "these developments are assumed to occur through proactive investments in research and development" [2], and adds that the future of solar cells in Canada is highly dependant on the research and development in this area.

Interest in PV research in Canada is evident through the efforts currently taking place in research centers at universities, where the majority of research and development is taking place. University level research underlying photovoltaic technologies in Canada is carried out in about 50 university laboratories, and about 200-250 full-time equivalent researchers are involved in PV solar cell R&D. [8]. The Natural Sciences and Engineering Research Council of Canada funding for PV research has doubled from 2006 to 2008, and is currently at $5 million per annum for 21 universities.

In addition to expanding research and development, the future of solar cells in Canada is also dependant on the successful commercialization of PV technologies. Major obstacles in realizing the transformation of the energy sector have been social and political, and therefore, as evident in Europe, policy implementation can instill significant and rapid changes. Canada is seeing some of these policy changes: In 2006 the Ontario Power Authority introduced the Renewable Energy Standard Offer Program, and later the 2009 Feed-In Tariff program for renewable energy.

The newly instilled environmental policies, coupled with growing environmental concerns and increasing interest in PV technologies highlight the importance of research in an attempt to move towards a cleaner future.

1.2 Why Organic Solar Cells?

One of the major drawbacks with solar cells is the high cost to efficiency ratio. The cost of traditional silicon solar cells remains high owing to expensive materials and manufacturing processes. Subsequently, third-generation solar devices such as polymer solar cells have increasingly become the focus

of research. The efficiency of these cells remains low: currently, the highest recorded efficiency is approximately 7.5% [9], in comparison to 25% for crystalline silicon [10]. The lower efficiency of these devices, however, may be compensated by lower production cost and simple fabrication methods. Conjugated polymers can be easily dissolved in common organic solvents, or even water [11]; this property makes them an attractive choice for use as ink in deposition processes in applications that require thin and homogeneous films [11]. Taking advantage of this property allows cheap and large area roll-to-roll manufacturing of solar cells, resulting in high-throughput, cheap production with clear advantages over classical semiconductor batch processing. While organic solar cells may not fully replace conventional silicon cells, there are certainly applications which benefit from the unique properties of organic PVs. Some of these applications include use on bendable substrates and fabrics such as on curtains, clothing, or in locations and architectures where cost is the overriding factor.

1.3 Motivation

In recent years, the main area of focus for improving organic solar cells has been the efficiency; however, stability of these devices is also an important factor for successful commercialization [12]. For this project, the main motivation is to perform an in depth study of initial performance as well as stability of organic PVs. Specifically, the focus of this study is to examine the effect of regioregularity and zinc oxide (ZnO) nanoparticles concentration on initial performance and stability of these devices.

Regioregularity is a measure of order in polymers, and is discussed in depth in Chapter 4 and Appendix A. Improving regioregularity has been previously reported to improve the performance of the solar cells [13]; however, stability of these devices has not been studied. Similarly, despite the reports of improved efficiency in hybrid ZnO-polymer solar cells [14–17], the stability of hybrid ZnO-polymer devices and degradation mechanisms have not been studied in much detail. The aim of this project is to methodically and quantitatively study the effect of regioregularity and ZnO addition on

aging properties of organic PVs.

The degradation mechanisms of organic solar cells, however, are not yet fully understood [1, 12, 18]. One reason for this may be the complication of the available conduction models [19]. Moreover, performance and degradation of organic PVs strongly depend on the processing conditions (see Section 2.3 for more information), and widely differing performance values are routinely reported for the same polymer [19]. As a result, a compact (or semi-compact) model that can be used for interpretation of experimental data and allows insight into underlying mechanisms of degradation is of great interest. Such a model is lacking for quantifying and analyzing degradation. A secondary motivation is therefore to apply semi-compact models that allow insight into the mechanisms responsible for improving power conversion and stability.

The primary contributions of this thesis can be summarized as follows:

- The degradation of P3HT:PCBM solar cells with regards to the extent of polymer regioregularity and ZnO concentration is quantitatively reported.

- Degradation characteristics of the devices are captured through semi-compact models which provide insight into the effect of varying regioregularity and ZnO addition. These models are used to relate current-voltage characteristics of the devices to the film properties and their subsequent change with annealing.

1.4 Thesis Outline

This thesis explores the performance and degradation of P3HT:PCBM films with respect to regioregularity and concentration of ZnO nanoparticles. Chapter 2 reviews principles of organic solar cells such as device architecture, light to electrical current conversion, fabrication parameters and optimization, and areas of current research. The fabrication, testing and characterization strategies for this project are described in Chapter 3. Chapter 4 studies the effect of varying the polymer regioregularity on device perfor-

mance and durability. In this chapter, the mobility edge model is introduced in detail. Chapter 5 studies the effect of ZnO addition to the P3HT:PCBM films, and examines the performance and stability of these devices. Finally, Chapter 6 presents a summary of the work and comments briefly on the proposed future direction of this investigation.

Chapter 2

Literature Review

The following sections give an overview of the state of technology in the organic PV field. The operating principles of organic PVs are introduced including device architecture, principles of incident solar irradiation conversion to electrical current, a description of conduction models, an overview of hybrid ZnO-polymer solar cells, fabrication optimization, and current research efforts.

2.1 Basic Principles

In polymer chains, the overlapping p_z orbitals of the co-planar polymers result in conjugated systems which act generally like semiconductors. Conjugation allows delocalization of π electrons across all the adjacent aligned p_z-orbitals and results in a system of alternating single and double bonds of sp^2-hybridized carbon atoms. Conjugation allows the polymer chain to lower its energy, and an energy gap opens between the highest occupied molecular orbital (HOMO) and the lowest unoccupied orbital (LUMO) [20]. The band gap becomes smaller with increasing number of repeat units as predicted by distortion theory [21]. Upon light absorption, electrons are excited from the bonding π into the anti-bonding π^* band.

The schematic of a polymer solar cell is displayed in Figure 2.1. The photoactive layer is sandwiched between a transparent electrode (usually indium tin oxide (ITO)) and an aluminum back electrode. Illumination takes place from the transparent ITO side of the device. The two electrodes may be further modified by the introduction of a PEDOT:PSS (poly[3,4-(ethylenedioxy)thiophene]: poly(styrene sulfonate)) coating on the ITO side in order to improve the extraction of holes and smooth the ITO surface [22].

The photoactive layer is composed of a hole-conducting donor polymer and an electron-conducting acceptor. The most commonly used hole-conducting, donor-type polymer is P3HT (poly(3-hexylthiophene-2,5-diyl)). Typically, the electron-conducting acceptor is a soluble derivative of C60, called PCBM ([6,6]-phenyl C61-butyric acid methyl ester).

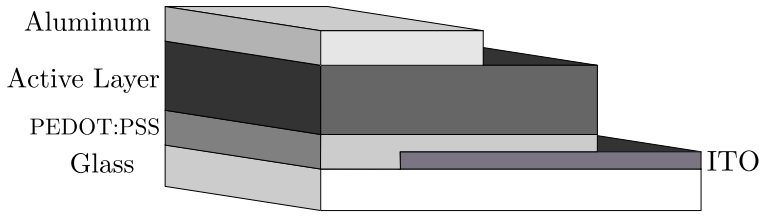

Figure 2.1: Schematic design of an organic solar cell

In organic solar cells, the incident solar irradiation conversion to electrical current can be divided into a five-step process: the first step is the creation of an exciton (bound electron and hole) after incident light absorption by the organic material. The second step involves diffusion of exciton inside the organic material to reach the D/A interface. The exciton splits-up into free holes and electrons at the D/A interface during the third step. Free charges are then transported through the sample and are collected at the electrodes.

Possible architectures for the photoactive layer include single layer, bi-layer, or blends. Single layer cells consist of only one semiconductor material and depend on charge separation at the rectifying Schottky junction between one of the electrodes and the semiconducting material. These cells are inefficient due to low light absorption by the single organic material and high recombination losses. Double layer cells use two different semiconducting materials as donor and acceptor material: the exciton is dissociated at their interface. Bi-layer devices benefit from separated charge transport layers that reduce the recombination losses [1]. However, photoexicton disassociation can only happen close to the junction, and the active zone is therefore limited by the small exciton diffusion length. This limitation can be removed

through the concept of the bulk heterojunction (BHJ), where the donor and acceptor materials are intimately blended throughout the bulk [23, 24]. The donor/acceptor (D/A) interface extends over the entire volume, and as a result, excitons do not need to travel long distances to reach the D/A interface, and charge separation can take place throughout the whole depth of the photoactive layer. Consequently the bulk heterojunction concept has led to major improvements of the photocurrent.

The following sections describe the light conversion to electricity in more detail, and cover light absorption, exciton diffusion, exciton separation at the D/A interface, charge transfer and collection at the electrodes.

2.1.1 Absorption

Upon incident light absorption, a bound electron-hole pair known as an exciton is created within the photoactive layer of a polymer solar cell. While silicon has a band gap and onset of optical absorption spectrum of around 1.1 eV (able to capture solar spectrum below 1100 nm, or about 77% of AM1.5G), most organic semiconducting polymers used today in PVs capture only the portion of the solar spectrum below 650 nm (larger than about 2 eV, or about 30%) [20]. The AM1.5G spectrum in comparison with the absorption range of P3HT and PCBM are demonstrated in Figure 2.2.

Despite the small range of wavelengths over which absorption takes place, the absorption coefficients for organic materials are comparatively high (about $10^5 \mathrm{cm}^{-1}$) and allow for efficient absorption even in very thin active layers [20].

2.1.2 Exciton Diffusion

Once the exciton is generated, the electrostatic attraction between the electron and hole keeps them bound to each other. The electron-hole pair remains localized on a few polymer repetition units or a molecule [11].

The exciton diffusion length is the parameter that accounts for the efficiency of the diffusion of the exciton in the organic material. Larger diffusion length corresponds to a greater probability that the exciton reaches the D/A

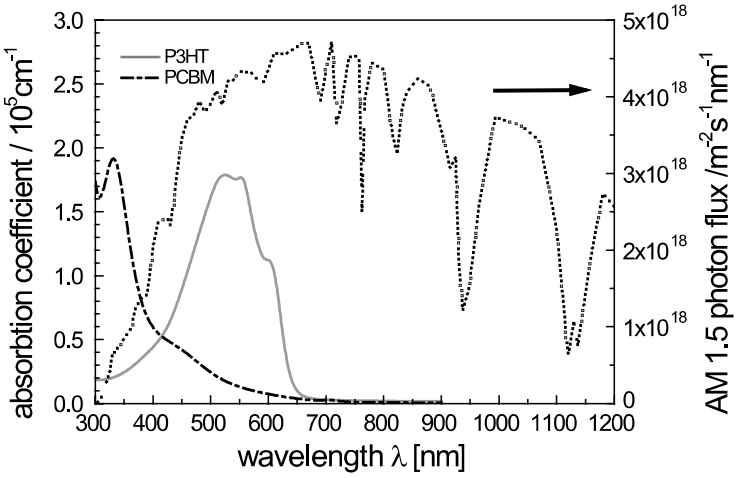

Figure 2.2: Absorption coefficients of P3HT and PCBM shown together with the AM 1.5 standard solar spectrum. Data used for generation of this graph was taken from [20], with permission.

interface, in turn increasing the probability of free electrons and holes forming. Diffusion lengths of organic materials are generally limited to about 5-20 nm [25–27]; therefore, the acceptor and donor material should be as close to each other as possible for the charge association to take place efficiently. If an exciton does not reach the D/A interface to be separated into its component free electron and hole, it eventually recombines [11].

2.1.3 Charge Dissociation

In this step the positively charged hole remains on the donor material whereas the electron becomes transfers to the acceptor [20]. This is schematically depicted in Figure 2.3. Exciton dissociation energies required to overcome the binding mechanism range between 0.1 and 1 eV [28, 29].

2.1.4 Charge Transport

Once separated, charges need to travel through the materials towards electrodes. Charge mobilities of organic polymers are typically low, and as a

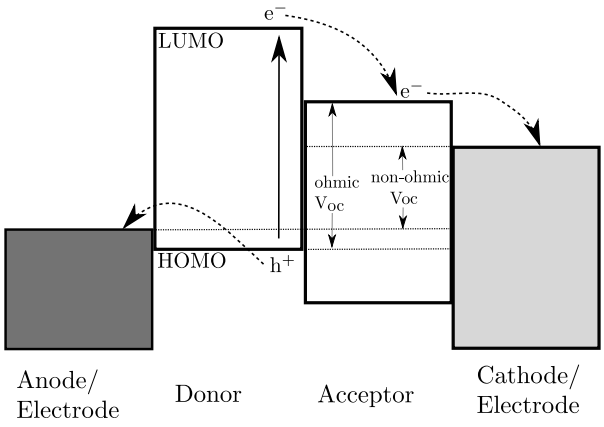

Figure 2.3: Electron and hole dissociation and transfer from an energetic perspective. Open circuit voltage depends primarily on molecular energy levels which are limited by the contact properties. In non-ohmic contacts, the voltage is limited by the difference of work functions of electrodes, as described in Section 2.1.5

result, charge recombination becomes a competing mechanism with charge collection and reduces photocurrent [30].

In organic polymers, electron-phonon coupling results in the creation of polarons, which cause the lattice to re-organize in order to allow the structure to energetically relax; these polarons may be regarded as defects in conjugated polymer chains [1]. Such defects in essence stabilize the charge, and the charge traps itself as a consequence. As a result, transport is generally dominated by a hopping process from one localized state to the next, instead of band transport found in crystalline semiconductors [1].

The hopping model as developed by Vissenberg and Matters [31] assumes conductivity in the polymer is equivalent to transport through a resistor network. In this network, the nodes have different energies according to the density of states (DOS). The percolation criterion through the network is then related to the temperature, position of the Fermi level, and the density of trap states [19]. The exact analytic treatment of carrier hopping in energetically and spatially arbitrary material is notoriously difficult [32].

Adding to the difficulty is that the degree of structural order may effect the charge transfer mechanism even within the same class of polymer, and the structural order strongly depends on the processing conditions (see Section 2.3). As a result, widely differing mobility values are routinely reported in literature for essentially the same polymer [19]. Because the electronic structure of semiconducting polymer films is not well understood, a semi-compact model which allows insight into transport properties becomes very useful.

Street et al.[19, 33, 34] have proposed the use of a mobility edge (ME) model. They have reported that based on the fit to the experimental data, the ME and hopping models are comparable, and in fact difficult to distinguish [19]. The ME model assumes that there is a defined energy (the mobility edge) in the DOS that separates mobile states from localized states. Trapped carriers may become temporarily mobile by excitation to the mobile states.

For studying the transport in organic materials, it is important to also take note of the unbalanced hole and electron mobilities. Electron-hole imbalance causes holes to accumulate at the immediate vicinity of the anode, in particular at high positive voltages. The hole conduction through the space charge region is therefore a bottleneck for conduction. The space charge limited current (SCLC) in trap-free conducting materials can be described by the Mott and Gurney model of space charge limited current. However, for organic polymers, the influence of traps must be taken into consideration [35].

2.1.5 Contacts

The final step is the charge collection at the electrodes. The open circuit voltage is limited primarily by molecular energy levels [36, 37]; however, the properties of the contact can also limit this voltage. The maximum V_{oc} is equal to $E_{\mathrm{LUMO}}^{\mathrm{acceptor}}$ - $\mathrm{E}_{\mathrm{HOMO}}^{\mathrm{donor}}$. In the case of ohmic contact, the negative and positive electrodes match the LUMO level of the acceptor and the HOMO level of the donor, respectively. As illustrated in Figure 2.3, if the Fermi

levels of the anode and the cathode are pinned to $E_{\mathrm{HOMO}}^{\mathrm{donor}}$ and $\mathrm{E}_{\mathrm{LUMO}}^{\mathrm{acceptor}}$ then open circuit voltage is $V_{\mathrm{oc}} = \Phi_{\mathrm{anode}} - \Phi_{\mathrm{cathode}}$ [1], where Φ is the work function of the electrode. When there is a non-ohmic contact V_{oc} becomes equal to $\Delta\Phi_{\mathrm{electrodes}}$.

This simple relationship, however, can differ significantly from experimental observations. The band-bending at the ohmic contacts reduces this open circuit voltage (around 0.2V for each contact)[38]. Moreover, the energy levels of the contacts depend critically on the possible formation of interface dipoles [20, 39, 40].

2.2 Hybrid Solar Cells

Hybrid solar cells combine the unique properties of inorganic semiconductors with film-forming properties of conjugated polymers: organic materials are usually inexpensive, easily processable, and their functionality can be tailored by molecular design and chemical synthesis [41, 42], and inorganic semiconductors are stable, possess tunable band-gap and absorption/emission spectra as well as high intrinsic carrier mobilities [14, 43].

One extensively studied material system among the nanocrystal-polymer blends is zinc oxide (ZnO). Zinc oxide is a promising semiconductor for use in solar cells due to high electron mobilities [14], and solubilities in organic solvents [44]. Several mechanisms are reported for being responsible for the power conversion efficiency of hybrid solar cells in the literature. Blending crystalline ZnO nanoparticles in bulk heterojunction semiconducting polymers may dissociate the excitons formed at the interfaces between organic and inorganic semiconductor more efficiently [14]. Additionally, the conduction band edge position of ZnO is similar to aluminum (Al), which can improve the performance of the device by decreasing carrier recombination at the electrode [15], and act as an effective contact for electron selection at the Al electrode [45]. Moreover, certain concentrations of ZnO nanoparticles may improve the formation of percolation pathways for electron transport [16]. Even though the absorption of ZnO in the visible region is insignificant, embedding ZnO nanoparticles in bilayer PV cells may also result in photon

scattering mechanisms which may enhance the absorption of the film [17].

2.3 Device Fabrication and Operation

A heterojunction can be realized in several ways. The most straightforward approach is to mix the donor and acceptor materials and spin-coat the solution on top of an electrode (ITO covered glass, for example) [46]. The following subsections discuss different parameters to be taken into consideration for the fabrication of organic solar cells, and are used as guidelines for fabricating devices in this project.

Thickness: Thicker layers of active material improve the photon absorbtion, however, due to the short diffusion lengths of these materials, sample thickness must remain relatively thin [47]. In the case of the P3HT/PCBM system, about 300nm layers maximize absorbance, but the optimum performance of P3HT/PCBM devices is often observed in active layers with thicknesses as much as half of this value [48, 49].

Solvent: The extent of solubility of organic materials in the solvent influences the morphology, donor/acceptor interfacial area [50] and photocurrent generation [51]. P3HT and PCBM are highly soluble in in chlorinated solvents, and most of the reported P3HT:PCBM films in the literature are prepared using chlorine-based solvents such as chlorobenzene (CB), and dichlorobenzene (DCB) [52, 53].

Drying Time: Dissolving the the organic material in a solvent with a high-volatility temperature under elongated drying times optimizes phase segregation during the solvent evaporation process and results in the formation of continuous pathways for electron and hole carriers and increased the interface area between the phases [50, 54].

Blend Ratio: The blend ratio influences the microstructure of the active layer. The optimum morphologies have been reported to occur at a 1:1 ratio of the P3HT:PCBM composites [55, 55, 56].

2.4 Current State of Research

Organic materials are by nature more susceptible to chemical degradation than inorganic materials [18]. While several degradation mechanisms have been identified so far, the issues with stability are not yet fully understood [1, 1, 12, 18]. A general understanding of these mechanisms can aid with the fabrication process, and some of these mechanisms are described below.

Temperature causes the films to lose the optimized form; the constituents can unmix, recrystallize, chemically react, reorient or become isotropic depending on the glass transition and melting temperature of the organic material [57]. High transition temperature materials may therefore improve the stability [1].

Isolated molecules under light can degrade due to effects of photochemistry such as in the formation of unwanted photo-isomers or photo-products [58]. Photochemical degradation can be reduced by molecular engineering, for example by designing conjugated molecules that do not give rise to photoisomers [1].

Water may contain mobile ions and can act as an electrolyte, and favor electrochemical reactions such as oxidation or reduction at the interfaces between the constituents under bias [59]. Moreover, water is a bad solvent for most organic materials and favors segregation in blends and mixtures. The solution is to remove water and prepare the compounds in a water-free atmosphere. Other encapsulation and protection methods against moisture includes plastic films and coatings [1].

Oxygen may oxidize the material, or act as an electron trapping center [1]. One solution to stabilize organic solar cells against oxygen is to use small molecules which are more resistant to O_2. Oxygen diffusion reduces due to a more compact molecular packing. In general, fabrication of organic solar cells must take place under a controlled atmosphere followed by encapsulation of the devices [1].

Diffusion can occur at interfaces in solar structures– for example from metal or semi-metal electrodes to the polymer films– especially when concerning a Schottky junction between the active film and metallic electrodes

[60]. Indium from ITO has been documented to diffuse into the electronic polymers, and degrading performance [61]. Diffusion at the interfaces can be shielded by interfacial layers made of densely packed small molecules.

2.5 Conclusion

This chapter presented a brief summary of the working principles of BHJ organic solar cells based on P3HT:PCBM. The performance of the solar cells is highly dependant on the morphology of intercepting donor/acceptor networks, and several parameters influence morphology during fabrication. These parameters were discussed, and are used further in the upcoming chapters as rationalizations for the chosen fabrication methods. The order of P3HT polymer was discussed, which can be influenced through the regioregularity of the polymer. Moreover, based on the working principles, some of the advantages of hybrid ZnO-polymer were described. The models describing the transport of carriers, in particular the mobility edge model, were also briefly introduced. The following chapters use these principles to fabricate devices and analyze the results.

Chapter 3

Fabrication and Testing Methods

This chapter focuses on describing the fabrication process of P3HT:PCBM devices using 93% and 98% regioregular polymer as well as ZnO-polymer devices. In addition to bi-carrier devices, the method of fabrication of single carrier (hole only and electron only) devices are also included.

The active area of each devices is 0.2 cm^2. For each experiment, a minimum of 6 devices are fabricated. All devices are stored in a glove box until testing. The glove box was operated under O_2 and H_2O levels < 0.1 ppm. For $I - V$ measurements, devices were placed in a home-built holder under vacuum.

3.1 P3HT:PCBM Devices

Figure 2.1 shows the schematic of the devices. Indium tin oxide (ITO) (Delta Technologies, 25 $\Omega/\square$) is used as the transparent electrode. A layer of PEDOT:PSS (Clevios P VP Al 4083, HC. Starck) [22] is used for hole blocking on the slides. The active area consists of P3HT purchased from Rieke Metals (93% Regioregular MW=50,000 g/mol) and PCBM (purchased from Aldrich). The cathode is made from Aluminum.

ITO is first masked by Kapton tape (DuPont) and etched from the middle of the substrate using a solution of 20 wt% hydrochloric acid. The slides are cleaned in acetone, isopropanol and water and wiped out with kimwipe to remove all glass particles remaining from cutting. The substrate is then sonicated in isopropanol for 20 minutes at 50°C followed by acetone sonication at 50°C and in a solution of ammonia and water. The substrate is then

sonicated in deionized water for 20 minutes.

PEDOT:PSS is filtered through a 0.45 μm PP syringe filter and is spin coated on the substrate at 3000 rpm resulting in a 40±10 nm layer, as verified by a Fimetrics thickness measurement device. The PEDOT:PSS layer is then annealed in an oven at 140°C for 10 minutes. Immediate baking is required in order to minimize the effect of water on the performance of the devices: PEDOT:PSS can react with ITO in the presence of water. This reaction may change the ionization potential of ITO, and cause diffusion of indium ions into the PEDOT:PSS layer, which lowers the efficiency of these devices [62].

For the semiconductor layer, the P3HT and PCBM solution is prepared in the glove box by mixing a 1:1 wt ratio of P3HT and PCBM in dichlorobenzene, (20mg/500mL of DCB for each) which are stirred on the hot plate at 50°C for 2 hours. The two solutions are then further stirred and heated overnight at 40°C. The solution was then filtered through a 0.45 μm PP Syringed filter. A 180 ± 20nm layer of P3HT:PCBM is achieved by spincoating at 100 rpm (1 s), 300 rpm (5 s), and 1000 rpm (15 s). The layer is then dried slowly over 45 minutes under a petri dish. Slow drying of the semiconductor polymer layer allows the P3HT polymer to crystalize and stack more effectively for a better electronic conduction [63].

The cathode consists of 100nm of Al thermally deposited through a shadow mask on the active layer after evaporating 20nm of calcium [62].

3.2 Highly Regioregular Devices

The fabrication of these devices is identical to the control 93% regioregular P3HT:PCBM devices described above, with the exception of using highly regioregular P3HT (>98%, MW=64,000 g/moland) as purchased from Rieke Metals.

3.3 ZnO-Polymer Devices

The fabrication of these devices is identical to the P3HT:PCBM devices with the exception of adding ZnO nanoparticles to the active film.

For the fabrication of the ZnO, p-type (100) oriented silicon substrates are used. Substrates are cleaned in hot acetone and isopropyl alcohol (IPA) followed by standard RCA1 and RCA2 cleaning treatments. Hydrofluoric acid (HF) dip is used to remove the native oxide. Gold nanoparticles are used as catalyst for vapor liquid solid (VLS) growth of ZnO nanowires. Hydrogen terminated Si substrate is immersed in gold colloid solution for 2 min while $1\mu L$ of 49% HCl is added to the colloidal solution, which results in an overall pH of 2-3. Then ZnO nanoparticles are grown in a horizontal tube furnace using high purity, 99.999% Zn powder as precursor. The furnace is then heated up to 700°C with a slope of 50°/min and under a constant flow of 100 sccm comprising 2% oxygen and 98% argon. Zinc crucible is placed in the center of the tube; the silicon substrate was 10-20 cm away from the precursor.

After ZnO was synthesized, the substrate was moved into the glove box, and 20mg of ZnO was added to 1ml of distilled DCB. The powder was then dissolved by stirring for 24 hours followed by high power sonication for 5 hours, and subsequently filtered though a 220nm PP syringe filter. Two solutions were made, one consisting of 5-vol% of ZnO in DCB solution, and the other of 10vol% ZnO in DCB.

3.3.1 Electron-only and Hole-only Devices

Hole-only and electron-only devices are fabricated using electrodes that either suppress or allow the injection of electrons or holes, respectively. Top electrodes for hole-only devices were fabricated by evaporating palladium on the devices; the overall configuration was ITO/(PEDOT:PSS)/P3HT:PCBM/Pd. The configuration of electron-only devices was Ag(100 nm)/P3HT:PCBM/Al(100 nm) [64, 65].

3.4 Testing

For testing of the devices, the following methods are utilized:

Ultraviolet visible spectroscopy (UV VIS): Light absorption is studied using ultraviolet to visible light at wavelengths 200-800nm. In UV-Vis absorption spectroscopy, the optical property of the materials is a function of wavelength, and absorbance is described by the Beer-Lambert law as shown in Equation 3.1:

$$A = -\log(T) = -\log(\frac{I}{I_0}) = \epsilon c L \tag{3.1}$$

In the above equation, A is absorbance, T is transmittance, I_0 and I are the intensity of the incident light and the transmitted intensity respectively at a given wavelength, L is the sample thickness, and c is the concentration of the absorbing species. For each species and wavelength, ϵ is the extinction coefficient, and is a fundamental molecular property. The wavelength of the incident light was changed by computer-controlled monochromator.

Voltage-Current Measurements: Light and dark current-voltage characteristics are measured using a semiconductor characterization system (KEITHLEY 4200, Keithley Co. Ltd.). Light characteristics are measured under standardized air mass 1.5 solar simulated light irradiation of 100 mW·cm^{-2}. The AM1.5G illumination is equal to the solar spectrum at earth's surface when the sun is at an angle of 48.19° from its zenith, and is incident on a south-facing surface (in the Northern Hemisphere) that is mounted at 37° to the horizontal [66]. A xenon lamp (300 W, 6258 Newport) equipped with an AM1.5G filter is used as the white light source. The optical power is 100 mW·cm^{-2}, measured using a broadband power meter 841-PE (Newport) equipped with an Ophir thermal detector head (3A-P-SH-V1).

Transmission electron microscopy (TEM): TEM is a technique for

material characterization with nanometer-scale spatial resolution. transmission electron microscopes operate similarly to optical microscopes, but using electrons instead of light; the smaller wavelength of the electrons makes it possible to view objects on the order of a few nanometers with high resolution. A source at the top of the microscope emits the electrons into the microscope column under vacuum. The electrons are focused into a very narrow beam, and travel through the specimen; a fraction of the electrons diffract or scatter depending on the density of the material. The remaining electrons hit a fluorescent screen at the bottom of the microscope, giving rise to a 2-dimensional shadow image according to the density of the specimen. The most common mode of operation for a TEM is bright field imaging. In the case for the BHJ samples, regions with a higher degree of crystallinity will appear dark, and less dense regions in the beam path will appear bright.

Bright-field TEM images for studying the morphology are captured with a Hitachi 8100 system. Films are created as discussed in Section 3.1. Immersing the samples in water results in the film separating from the substrate, and floating on the surface of water. The films are carefully removed from water and placed on a 500-mesh TEM copper grid. For capturing TEMs of the ZnO nanoparticles, drops of ZnO mixed in DCB were placed on mesh copper grids, and dried.

Optical microscopy: The morphology is also studied using optical microscope for features of the morphology that are $> 1\mu m$. An Olympus LEXT OLS4000 Laser Confocal microscope was used to examine the active layer morphology when the surface features are $> 1\mu m$, and allowed for rotation of the sample and studying the surface morphology.

3.5 Photovoltaic Characterization

The dark characteristics of the organic solar cells result from the superposition of bulk transport mechanisms with organic/electrode interfacial electrical properties [1], as shown in Figure 3.1. As discussed in section 2.1.4, in high voltage-high current regimes, the unbalanced hole and electron mo-

bilities result in the current density being associated with the space charge limited current (SCLC) law.

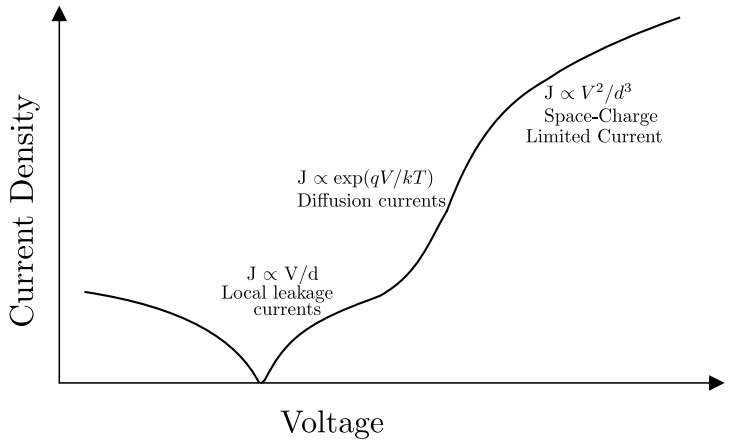

Figure 3.1: $I - V$ characteristics showing different domains [1]

A typical current-voltage $I-V$ curve of a polymer solar cell under illumination is shown in Figure 3.2. The following sections describe the parameters as noted on the figure in more detail.

Short Circuit Current(I_{sc}): the measured current of the solar cell at zero applied voltage, and is a function of illumination.

Open Circuit Voltage(V_{oc}): the maximum voltage available from a solar cell, which occurs at zero current.

Maximum Current and Voltage (I_{mp} & V_{mp}): current and voltage at which the resulting power reaches the maximum absolute value, and represents the condition where the solar cell delivers maximum power to an external load: this is called the maximum power point.

Fill Factor (FF): the ratio of the maximum power to the external short- and open-circuit values, respectively:

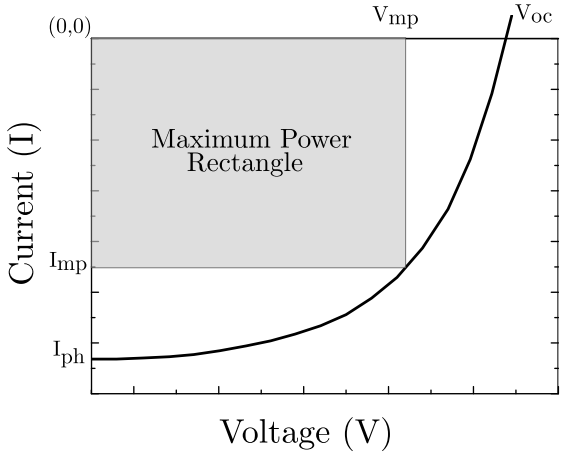

Figure 3.2: Current versus applied voltage characteristics of a solar cell

$$\begin{aligned} FF &= \frac{P_{\max}}{I_{\text{sc}} \times V_{\text{oc}}} \\ &= \frac{V_{\max} \times I_{\max}}{V_{\text{oc}} \times I_{sc}} \end{aligned} \tag{3.2}$$

Ideally, the fill factor would be unity, but losses due to transport and recombination result in values between $0.2 - 0.7$ for organic photovoltaic devices.

Photovoltaic Efficiency(η): efficiency is defined as the ratio of the maximum electric power extracted to the illumination power intensity G times the surface A of the module:

$$\eta = \frac{P_{\max}}{A \times G} \tag{3.3}$$

3.6 Accelerated Testing

For studying degradation mechanisms, accelerated testing is used. The decay process, which may be chemical in nature, has been shown to follow an

Arrhenius-type model where the rate of decay is determined by an exponential (or stretch exponential) function [67]. In the case of organic solar cells, accelerate testing is based on artificially shortening the lifetime of the devices by increasing the temperature. De Bettignies et al. [68] have shown in accelerated lifetime studies for P3HT:PCBM that the decrease in short circuit current after 200h at 60°C corresponds to 1000 h at 25°C. In this study of degradation mechanisms, all devices are thermally annealed for 1hour at a time at 140°C. This value was chosen based on common aging temperature in literature [64, 69].

Chapter 4

Degradation in Regioregular P3HT Bulk Heterojunction Organic Solar Cells

Since the emergence of polymer:fullerene bulk heterojunction solar cells, optimization efforts have been heavily focused on improving the nanoscale morphology of the photoactive films [70, 71]. In bulk heterojunction solar cells the morphology of the D/A interpenetrating networks is essential for both exciton dissociation and charge transport. It has been shown that one way of optimizing the morphology of the P3HT:PCBM networks and improving charge transport is through enhancing molecular packing [72]; this can be done through increasing the degree of regioregularity (RR). Regioregularity is the percentage of monomers in the head-to-tail configuration rather than head-to-head [13]. For more information on the definition of regioregularity, see Appendix A.

Previously, we have investigated the effect of annealing on the performance of P3HT:PCBM devices with different (93% and 98%) regioregularities, the results of which have been published along with the findings of this chapter in [64, 65]. We compared different parameters of fabricated photovoltaic devices, including power conversion efficiency, absorption spectra as well as current-voltage characteristics, before and after annealing. We also studied the morphology of the films for different regioregularities using electron transmission microscopy. We found that higher RR P3HT devices initially have a better performance. This initial enhancement in performance with increased RR, however, does not hold with aging, as seen

in Figure 4.1. P3HT and PCBM are not miscible; over time, blends of the two may segregate, forming crystallized discontinuous microscopic domains of each polymer. Crystallization is reported to exclude PCBM from the ordered polymeric domains in bulk heterojunctions [73]. Crystallization-driven phase segregation is thought to be the main cause for a reduction in donor-acceptor (D/A) interfacial area [73], which in turn lowers the performance of solar cells.

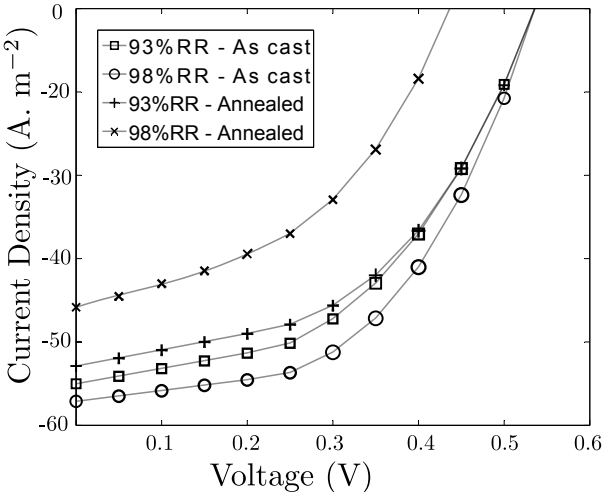

Figure 4.1: $J - V$ characteristics of devices with different regioregularities, for as-cast and annealed conditions.

In order to gain a better understanding of degradation mechanisms in regioregular P3HT:PCBM devices, electron- and hole-only devices are fabricated for this project. For more information on fabrication and testing of these devices, please see Chapter 3. Electron and hole mobilities are extracted using the mobility edge (ME) model. The proposed model can be used to:

- Extract effective electron and hole mobilities at reference carrier densities, which enable a standard formalism for comparison of carrier transport in different films. This is useful for organic films, where

conduction depends non-linearly on carrier concentration and physical attributes of the devices [74].

- Relate experimental $I - V$ characteristics of the devices to material properties and electronic structure: this is beneficial as it formulates a method of identifying the effect of regioregularity with annealing time.

- Allow insight into the nature of conduction degradation: as discussed in 2.1.4, the density of localized states of the polymer influences the effective conductivity of the material. The proposed model captures sufficiently well the contribution of regioregularity to localized states with annealing, and can be used to estimate the energy distribution of the carriers, electron and hole mobilities, mobility degradation with the annealing time, and the effect of disorder-induced localized states on transport properties.

From the points above, it can be concluded that this semi-compact model is a powerful tool for capturing the aging characteristics of the polymer and the effect of regioregularity. The following sections describe this model in more depth, and drive an expression for effective mobility that takes into account the effect of localized traps on the space charge limited current.

4.1 Mobility Edge Model

In the ME model, it is assumed that the density of states (DOS) of the polymer is described by bands with exponential tails extending into the band gap, as shown in Figure 4.2. The essential property of this DOS is that it varies slowly with energy inside the band near the band edge, while it varies exponentially with energy inside the band gap. The mobility edge, $E_0 = 0$, is defined at the top of the band-like states. Thus, the localized states below the mobility edge are represented by an exponential tail [19]:

$$g(E) = \frac{N_t}{E_b} \exp\left(\frac{E}{E_b}\right) \tag{4.1}$$

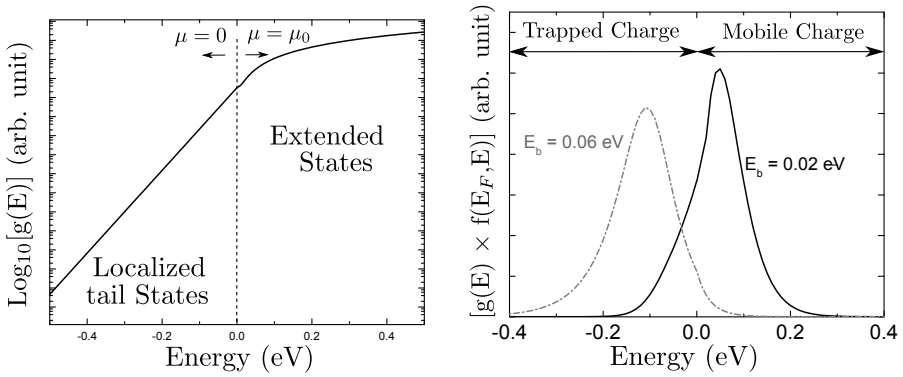

(a) Density of States (b) Carrier Density

Figure 4.2: DOS and carrier density graphs: a wider localized band tail E_b means more trapped carriers. Electrons at energies above the mobility edge E_0 are mobile and assumed to have a constant mobility equal to the band mobility μ_0, while electrons located at energies below the mobility edge have zero mobility.

where E is the energy, N_t is the total density of traps, k is the Boltzmanns constant, and E_b is the width of the exponential tail. In order to take into consideration the effect of traps on transport, the correlation between trap density and current density has to be found. Equation 4.2 shows an expression for the SCLC current density due to the carriers excited to the hopping transport band [75]:

$$J = q\mu_b N_b \kappa \left(\frac{\varepsilon}{qN_b}\right)^{\alpha} (V_D - V_t)^{\alpha+1}/t^{2\alpha+1} \tag{4.2}$$

where V_t is the onset of the power-law regime, q is the elementary charge, N_b the density of states in the transport band, μ_b the carrier mobility of the band, ε the dielectric constant, V_D the diode voltage, t the electrode separation, $\kappa = \alpha^{\alpha}(2\alpha+1)\alpha + {}^{1}/_{(\alpha+1)^{2\alpha+1}}$, and α is the power parameter. Equation 4.2 is derived from Poissons equation and charge conservation equations [76, 77].

As seen in Equation 4.2, the current-voltage characteristics follow a

power-law dependence on α. The power parameter, α, is a function of T_t (the characteristic temperature indicating the width of the exponential distribution) normalized by the ambient temperature, and is given as follows:

$$\alpha = \frac{T_t}{T} = \frac{E_b}{kT} \tag{4.3}$$

Equation 4.2 and 4.2.3 relate the power-law behavior to the trap density, by stating current is proportional to the width of the exponential tail, E_b, as seen in Figure 4.2. The $J-V$ characteristics can thus provide approximate, yet critical, information on the material properties, including an estimate for density of states and effective mobility that does not include device attributes. Therefore, α can be treated as a measure of trap density; the larger the α the higher the density of traps in the band tail. α is extracted from the power-law $J-V$ characteristics of the device, $J = k(V - V_t)^{\alpha+1}$. It follows that $J/g = (V-V_t)/(\alpha+1)$ where $g = \partial J/\partial V$. Therefore, to extract α, the slope of the J/g versus V curve can be used [75].

In order to find an expression for μ_{eff}, the relationship between the mobile density of carriers (n_{mobile}) and the density of trapped carriers (n_{trapped}) has to be found, and is described in Appendix B [74]. The expression for effective mobility can then be found according to Figure 4.2, and is summarized as the following [19, 74]:

$$\mu_{\text{eff}} = \mu_b \frac{n_{\text{mobile}}}{n_{\text{total}}} \tag{4.4}$$

By replacing Equation 4.4 in Equation 4.2, effective mobility can be extracted from measured $J-V$ characteristics:

$$J = q\mu_{\text{eff}} N_0 \kappa \left(\frac{\varepsilon}{qN_0}\right)^{\alpha} (V_D - V_t)^{\alpha+1}/t^{2\alpha+1} \tag{4.5}$$

where N_0 represents effective mobility at a reference carrier concentration

$N_0 = 2 \times 10^{16}$ cm^{-3} [74].

The effective mobility provides a standard formalism for comparison of mobility, and takes into consideration the disorder-induced localized states. Moreover, the expression for α relates the current-voltage behavior to the width of exponential band, and can be used to describe the energy distribution of the carriers and how the conduction varies as a function of regioregularity. The following sections use this concept to gain understanding into the nature of aging in regioregular polymer based solar cells.

4.2 Results and Discussion

In the following sections, effective mobilities are extracted and the relation between structural order and electronic conduction according to the ME model are explored. To understand the electronic properties, the analysis includes examining electron and hole mobilities, mobility degradation with respect to annealing time, and an estimation of energy distribution of the carriers. For more information on the fabrication method, please see Chapter 3.

4.2.1 Hole Mobility

Figure 4.3 shows the dark $I - V$ characteristics of the hole-only devices, fabricated using 93% and 98%-RR P3HT:PCBM blends, before and after 2 hours of annealing at 150°C. For the complete set of data, please see Appendix C

For the as-cast devices, the 98%-RR device shows slightly larger current than the 93% device. This can be attributed to the superior organization of P3HT domains, enhanced degree of crystallinity, and more efficient electronic conduction [64]. Neither degree of regioregularity or annealing seems to significantly effect hole transport. Figure 4.3(b) shows the J/g vs. V curves for all devices. The slope of this graph can be used to find the value of α, as discussed in Section 4.1. The extracted $\alpha = 0.1$ indicates that conduction is near-ohmic. Extracted hole mobility is 6.2×10^{-4} cm^{2}V^{-1}s^{-1} and

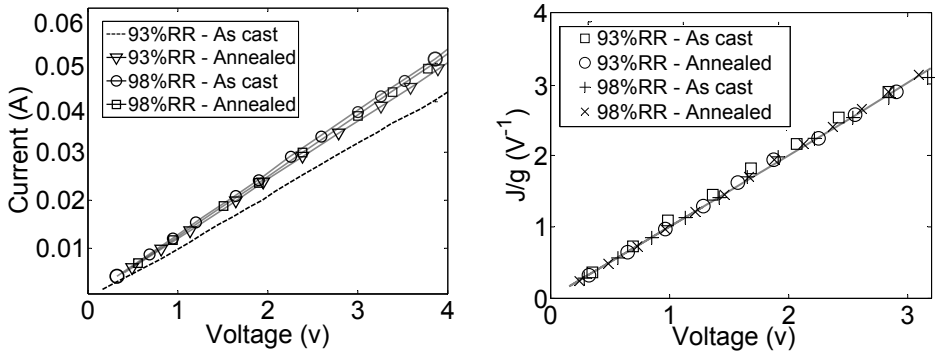

(a) Hole $I - V$ characteristics

(b) J/g vs. V: slope $= (\alpha + 1)^{-1}$

Figure 4.3: $I - V$ and J/g vs. V characteristics of hole-only 93% and 98% RR devices: $\alpha + 1 = 1.1$ and does not change significantly with annealing.

remains unchanged after annealing. Due to the insignificant changes with annealing and regioregularity, change in effective hole mobility is ruled out as the possible cause of the performance degradation.

The hole mobility in P3HT:PCBM blends is correlated with the degree of crystallization of P3HT, and because annealing encourages crystallization of P3HT, hole mobility is expected to increase with annealing [78]. The insignificant change in hole mobilities may be due to the already optimized morphology. This can be attributed to the dry annealing process: a slow rate of solvent evaporation assists in optimizing the morphology by controlling crystal growth of the P3HT. Therefore, after evaporation of solvent, an optimum morphology is already obtained for hole transfer.

4.2.2 Electron Mobility

Figure 4.4 shows the J/g vs V characteristics for the electron-only (a) 93% and (b) 98% devices. For the complete set of data, please see Appendix C

Comparing Figures 4.4(a) and 4.4(b) shows that the increase in α with annealing is more pronounced for 98%-RR devices. In the ME model, the power parameter α is a measure of trap density, and therefore, the increase in α suggests an increase in density of traps. The increase in traps may be

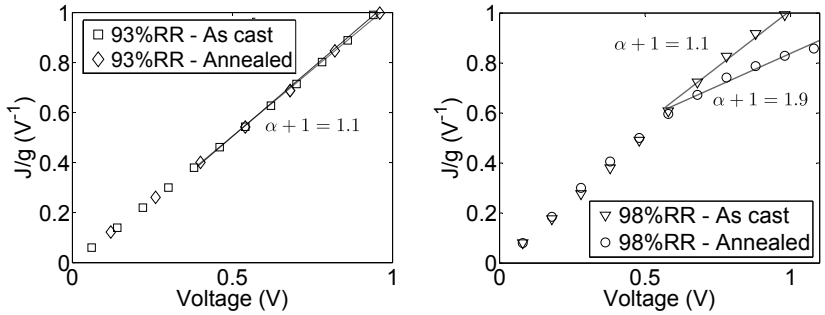

(a) 93%RR devices, as-cast and annealed

(b) 98%RR devices, as-cast and annealed

Figure 4.4: J/g vs. V characteristics of electron-only 93% and 98% RR devices, before and after annealing for 2 hours: the slope gives values for $\alpha + 1$, where $\alpha = T_t/T$: increase in α corresponds to an increase in the trap density.

due to a reduction in the continuity of the electron carrier phase [64], and may be attributed to the crystallization-driven phase segregation of 98%-RR P3HT. The phase segregation results in crystallization/exclusion of PCBM molecules from ordered domains, and result in trap generation for electron transport.

The formation of many needle-shape PCBM crystals has been studied before. We [64] have shown that thermal annealing induces the formation of many needle-shape clusters of PCBM crystals that are several tens of micrometers in length in the P3HT:PCBM blend films. Specifically, the phase segregation and formation of PCBM crystals are far more extensive in 98%-RR films than in 93%-RR films. These clusters increase phase separation, causing the electron mobility to decrease, and justifying the increase in the power parameter. For more information on the formation of PCBM clusters with age, please see [64].

Figure 4.5 shows the change in electron mobilities with annealing time as extracted using Equation 4.5. The electron mobility of the 98%-RR devices, initially larger than the 93%-RR devices, falls rapidly with thermal annealing.

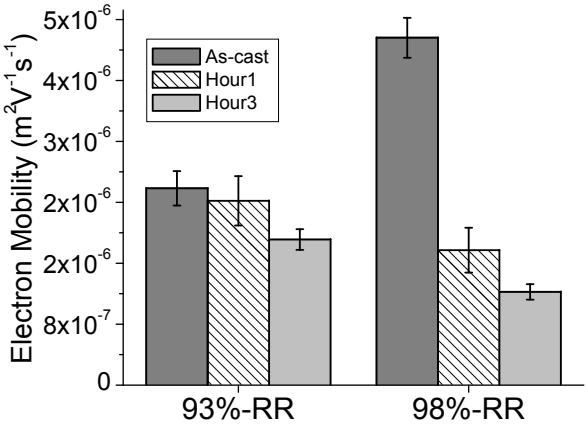

Figure 4.5: Extracted mobility values for 93% RR and 98% RR devices over annealing time: though initially the mobility for the 98%-RR devices is higher, the mobility falls with annealing more sharply than the 93%-RR devices. The sharp decline in electron mobility can be due to an increase in trap density as a result of phase segregation between P3HT:PCBM.

4.2.3 Density of States

The observed difference in the voltage dependence of α is used to approximately sketch DOS vs. energy, shown in Figure 4.6. For obtaining this graph, it is assumed that DOS varies gradually with energy inside the band near the band edge (D(E)$\approx$E^n [19]) while it varies exponentially with energy inside the band gap, as given by Equation , where the value of N_t is taken from literature [19]. The accuracy of this figure is limited due to the assumptions regarding the shape of DOS and the value of N_t. Despite the limited accuracy, this figure indicates that the band tail in the annealed sample is larger, which suggests the presence of more local traps in the band gap. This is reasonable: in 98% RR blends, the PCBM exclusion is aggressive with annealing, which results in interruption of bi-continuity of the networks and the large segregated phases can start acting like traps.

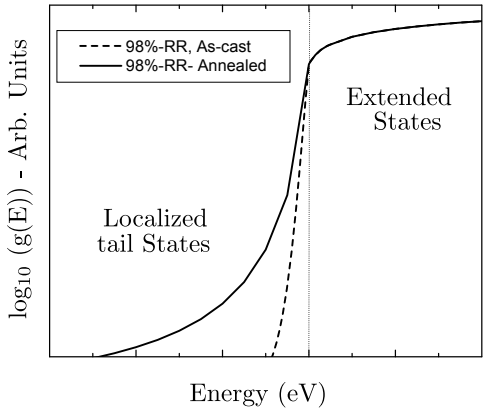

Figure 4.6: Difference between the shape of DOS vs energy graphs for 93%RR and 98% RR, at reference carrier concentration of $N_0 = 2 \times 10^{16}$ cm^{-3}, as previously reported in [74]

4.3 Conclusions

The effects of annealing and regioregularity on the charge transport characteristics of P3HT:PCBM photovoltaic cells are investigated. Hole mobilities are comparable for 93% and 98%-RR devices, before and after annealing, and therefore, the change in hole mobility is ruled out as a possible explantation for performance degradation. The electron mobilities for the 98%-RR devices experience a sharper decrease in comparison to the 93%-RR devices. This is reflected in the increase in the power parameter α in the mobility edge model. According to the ME model, the increase in α upon thermal annealing is attributed to an increase in trap states in the exponential tail for electrons. The increase in the trap density may be due to phase segregation in blends of 98%-RR polymer and PCBM. These results show that electron transport plays a critical role in the degradation of effective mobility of P3HT:PCBM solar cells.

Chapter 5

Degradation Mechanisms in Hybrid Zinc Oxide-Polymer Organic Solar Cells

Hybrid organic-inorganic photovoltaic cells combine the unique properties of inorganic semiconductors and conjugated polymers, as discussed in section 2.2. One attractive material among the crystalline nanoparticles for use in polymer blends is zinc oxide (ZnO), and has become the topic of recent focus. Despite the reports of improved efficiency in hybrid ZnO-polymer solar cells [14–16], the stability of hybrid ZnO-polymer devices and degradation mechanisms have not been studied in much depth.

The following sections aim to give an in depth overview of the effect of incorporating ZnO on the degradation of P3HT:PCBM devices. The devices are compared based on their current-voltage ($J-V$) characteristics, optical density and power conversion efficiency (PCE). Electron and hole mobilities are extracted for these devices and compared with annealing time. The morphology of devices with and without ZnO are investigated for as-cast and annealed samples. The following section describe each in more depth.

5.1 Results and Discussion

In order to investigate the underlying mechanisms that contribute to PV performance in ZnO-polymer solar cells, three sets of devices with ZnO concentrations of 0%, 5% and 10% are studied. For more information on fabrication and testing methods, please see Chapter 3. . The bars in the fol-

lowing figures represent the standard error for the results of each experiment; for each experiment, a minimum of 6 samples were fabricated and studied. For the complete sets of data for all tests, please see Appendices E-H. From the set of 6, the results for the top performing 4 samples are reported in the following section. This is done to remove outliers in a systematic way.

Figure 5.1 shows a plot of the current density-voltage ($J-V$) characteristics under illumination. The 5%-ZnO devices exhibit the largest short circuit current density (J_{sc}) as well as the highest efficiency and fill factor among all samples before annealing. Increasing the concentration past a critical point, however, lowers the performance as seen in the results for 10%-ZnO devices.

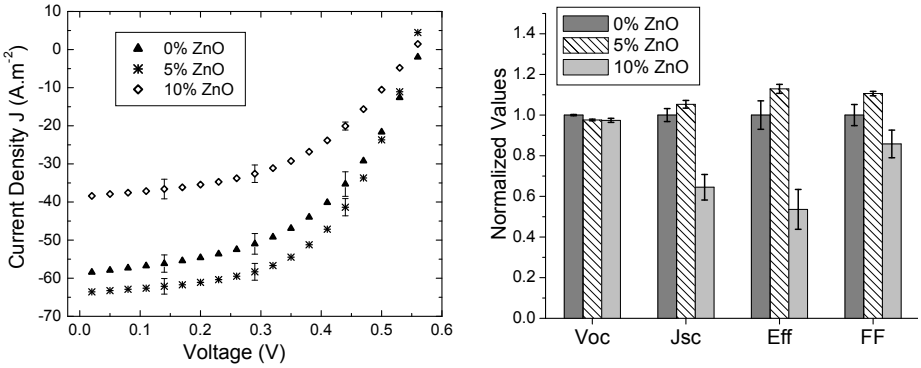

(a) $I-V$ for 0%, 5% and 10% ZnO devices (b) Normalized performance parameters

Figure 5.1: Performance characteristics of as-cast devices with various concentration of ZnO nanoparticles: the devices with 5%-ZnO show the highest short circuit current, fill factor and efficiency. The performance parameters in Figure 5.1(b) are normalized to the values of 0%-ZnO devices ($V_{oc} = 0.565V, J_{sc} = 58.57A \cdot m^{-2}, \eta = 1.69\%$ and $FF = 52.9\%$)

Not only does ZnO improve the performance, but it also increases the stability of the devices. As seen in Figure 5.2, the 10%-ZnO devices are the most stable, and the 5%-ZnO devices are not only more efficient, but also more stable than the 0% -ZnO devices. Accelerated aging for three hours results in the highest drop in efficiency for devices with no added ZnO, while the 10%-ZnO devices experience virtually no decline. The decline in the fill

factor is also largest for the 0%-ZnO and smallest for the 10%-ZnO devices.

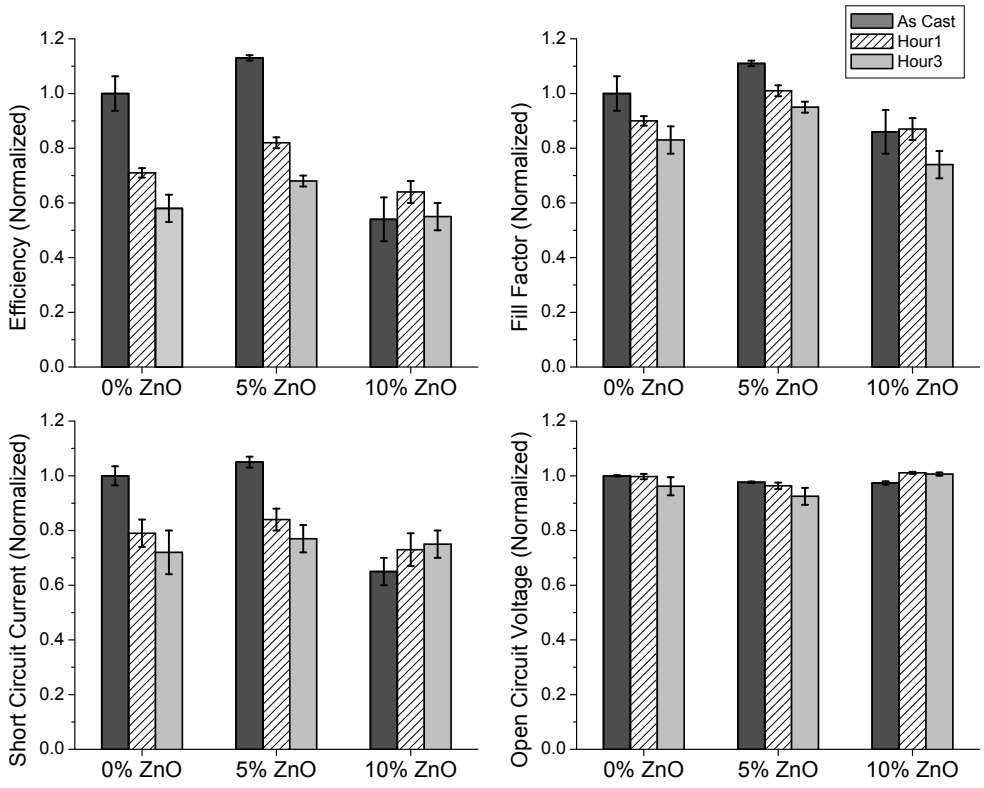

Figure 5.2: Performance parameters for devices containing different concentrations of ZnO nanoparticles, and their subsequent change with accelerated aging. The values are normalized to the values of 0% as cast ZnO devices ($V_{oc} = 0.565V, J_{sc} = 58.57A \cdot m^{-2}, \eta = 1.69\%$ and $FF = 52.9\%$).

In the following sections, the absorption spectra of the polymer film, photovoltaic characteristics, extent of recombination, charge transfer and the surface morphology are studied in detail in order to gain more insight into mechanisms that are responsible for the observed increase in efficiency of 5%- and stability of 10%-ZnO devices, with respect to 0%-ZnO devices.

5.2 Optical Property

The solid-state absorption spectra for the films containing as-cast 0%, 5% and 10% ZnO are shown in Figure 5.3.

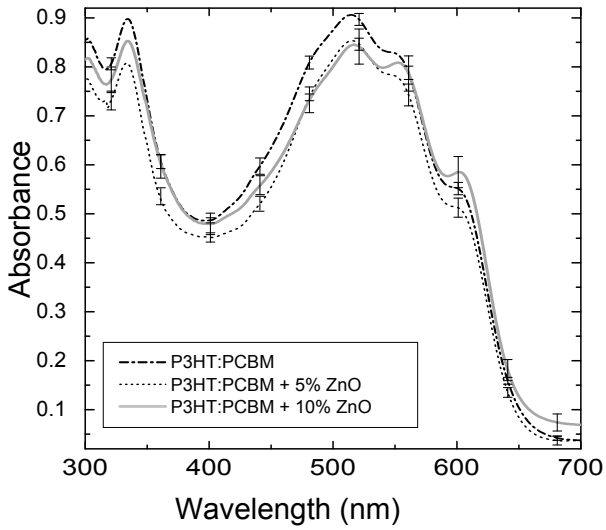

Figure 5.3: Absorption of devices containing various concentrations of ZnO

In this figure, the difference between the mean values of absorption for the 0, 5 and 10%-ZnO devices is not statistically significant, as shown by the overlapping values for standard error. Though the results are not conclusive, the mean of the 5% ZnO devices show slightly lower absorption in comparison to no-ZnO devices over the entire wavelength range. This may be due to dilution of P3HT-PCBM films by the addition of ZnO; the absorption of ZnO is minimal in the visible range [79]. Annealing does not effect the absorption of the devices. For the complete experimental data for the absorption, please see Appendix F. Despite similar or lower absorption, 5%-ZnO devices show higher short-circuit current, as seen in Figure 5.2. It can thus be concluded that absorption of the films is not responsible for the improved performance and stability of the devices containing ZnO.

5.3 Photovoltaic Characterization

The incident light absorbed by the organic material results in the creation of an exciton. If an exciton does not separate into an electron and hole, it eventually recombines [80]. After the exciton is dissociated at the D/A interface, free charges must travel to the electrodes to be collected; however the amorphous and disordered nature of these organic films hinders transport [11]. The following sections describe a model that relates these properties to the measured current-voltage characteristics. This model can then be used for examining performance and stability of the hybrid devices.

Figure 5.4(a) shows a typical equivalent circuit of a solar cell. Though this representation was primarily developed for inorganic solar cells, good correlation has been reported for organic solar cells. Waldauf et al.[81] have proposed this model to be used as an "expanded *pn* juntion". This model explains the pn-junction-like behavior on the device parameters and performance. The expanded *pn* junction takes into account the difference between the characteristics of bulk heterojunctions and metal-insulator-metal (MIM) model, which has previously been applied to BHJ devices. In the MIM model, the intimate mixture of acceptor and donor materials is treated as a homogeneous film, and unifies the parameters of both materials. The expanded *pn* junction model proposes that the exponential behavior depends on the properties of the two materials involved, and the observed characteristics is assumed to be an average of the behavior of the total D/A interface throughout the bulk. From the equivalent circuit, it can be derived that:

$$I = I_{\text{ph}} - I_s \left[\exp(\frac{qV + R_s I}{nkT}) - 1 \right] - \frac{V + R_s I}{R_{sh}} \tag{5.1}$$

where n represents the ideality factor of the diode, I_s represents the saturation current, q is the elementary charge, k is the Boltzmann constant, T stands for the temperature. R_s and R_{sh} are series and shunt resistances, respectively.

As seen in equation 5.1, the $J - V$ characteristic depend on the ideality

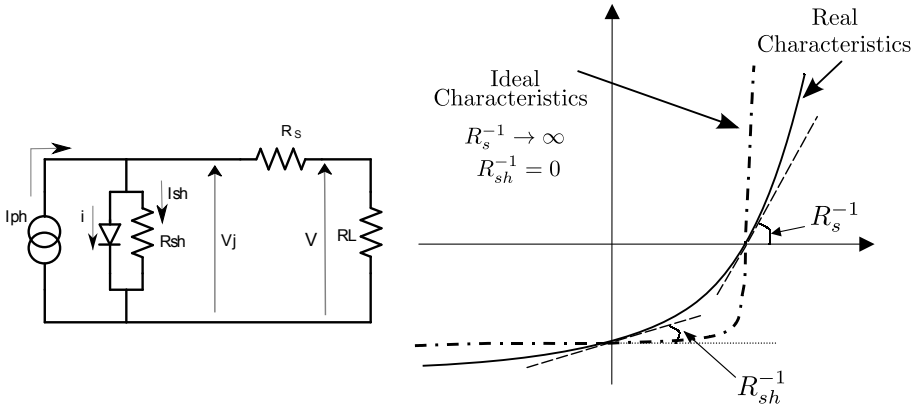

(a) Equivalent circuit (b) Effect of R_s and R_{sh} on $I - V$ characteristics

Figure 5.4: Comparison of ideal and real $I - V$ characteristics in terms of series and shunt resistances using the equivalent circuit for expanded pn junction model: R_s and R_{sh} are linked with the slope characteristics at $V = V_{oc}$ and $V = 0$ respectively.

factor n and the reverse saturation current J_s. The ideality factor reflects the recombination behavior where opposite charge carriers meet, i.e., at the D/A interface, and reflects the properties of the interface and the morphology [81, 82]. In organic BHJ devices, it is reported that a unity ideality factor corresponds to band-to-band recombination and an ideality factor of 2 arises from the generation-recombination mechanism, which requires states near the middle of the interface gap [83]. The saturation current J_s reflects the current caused by thermal activity; in the reverse bias region, this current is not affected by the magnitude of the bias, but changes with temperature. In other words, this current is a measure of the number of charges which are able to overcome the energetic barrier in the reverse direction.

The major contributions to series resistance R_s are the bulk resistance of the organic materials, resistance of the electrodes and the contact resistances between the electrodes and the organic material [84]. Shunt resistance takes into consideration the conduction through single polymer paths connecting the electrodes [81]; due the random nature of the bulk, continues paths of

either P3HT or PCBM may cause shunts between the electrodes. As seen in Figure 5.4(b), the series and shunt resistance change the slope characteristics at $V = V_{oc}$ and $V = 0$, respectively. The changes in the slope directly translate into changes in the fill factor and the efficiency of the cell.

The dark current is limited by values of shunt resistance at low currents and series resistance at high currents, and shows exponential behavior under moderate voltage. Saturation current and ideality factor can be found by fitting Equation 5.1 to the exponential part of dark voltage-current characteristics (see Figure 3.1). The values for shunt and series resistance can be found by fitting the $I - V$ characteristics to Equation 5.1 at low and high bias regimes, respectively. The following sections describe the extraction of diode parameters (i.e. saturation current and ideality factor), shunt and series resistances, and effective electron and hole mobilities. Similar to Chapter 4, the ME model is used to examine the effect of ZnO on trap generation and relate conduction to the density of localized traps.

5.3.1 Diode Behavior

The values for the ideality factor and saturation current are summarized in Table 5.1. The ideality factor increases with ZnO addition. This is reasonable: the diode ideality factor reflects the interface properties and BHJ morphology [81, 82], and ZnO may increase recombination in the organic-ZnO interface. The ideality factor also increases with annealing time. This may be due to the resulting phase segregation between P3HT and PCBM; as the total D/A interface area decreases, the ideality factor of the diode increases. The extracted values of n is consistent with the values reported in literature, and may imply the presence of generation-recombination mechanism [83]. The reduced value of $n < 2$ may be due to the presence of recombination centers that are not at the center of the gap, or may be due to electron-phonon coupling which may increase the sum of the two transition energies to values larger than the interface band gap [83].

The total D/A interfacial loss as a result of annealing in terms of film morphology is further discussed in Section 5.4.

	0%-Zn		5%-ZnO		10%-ZnO	
	J_s	n	J_s	n	J_s	n
As-cast	6.2E-9	1.54	4.3E-9	1.57	2.6E-9	1.62
Annealed 2hours	5.9E-9	1.61	4.4E-9	1.64	2.7E-9	1.65

Table 5.1: Values for current density (A.cm^{-2}) and ideality factor for 0%, 5% and 10%-ZnO devices, before and after annealing

Saturation current decreases with ZnO addition. This may be explained by studying the energy bands of the constituents, shown in Figure 5.5. The valence band edge of ZnO is at about -7.6 eV. This is much lower in energy than the HOMO energies of PCBM and P3HT (-6.1 eV and -5.2 eV, respectively). As a result, the presence of ZnO may reduce the hole carrier contribution to the saturation current density, and in effect reduce the saturation current by blocking holes.

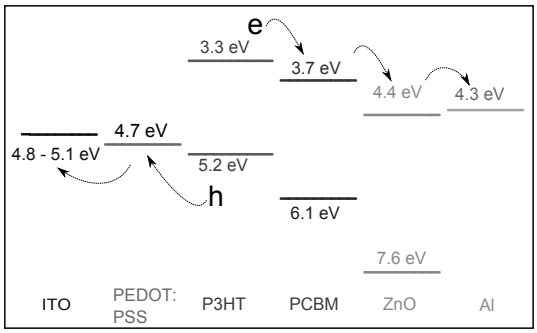

Figure 5.5: Energy band diagram for P3HT:PCBM devices with ZnO, indicating ZnO may improve hole blockage

5.3.2 Shunt and Series Resistance

In organic cells, shunt resistance may result from single polymer paths connecting the anode and cathode [81]. Under illumination, light induced charge generation ("photodoping") reduces the shunt resistance dramatically [81], and the bulk becomes loaded with a significant charge density. Examining

the values of shunt resistance shown in Figure 5.6 suggest that ZnO addition improves shunt resistance; this may be a secondary evidence that ZnO acts as a hole blocking barrier.

Despite showing lower initial values, however, the increase in shunt resistances for the 5% and 10% devices with annealing is comparable to the increase in shunt resistance of 0%-ZnO devices, as seen in Figure 5.6. This implies change in shunt resistance is not responsible for the stability of the devices containing ZnO - for measurements suggesting stability, please refer back to Figure 5.2.

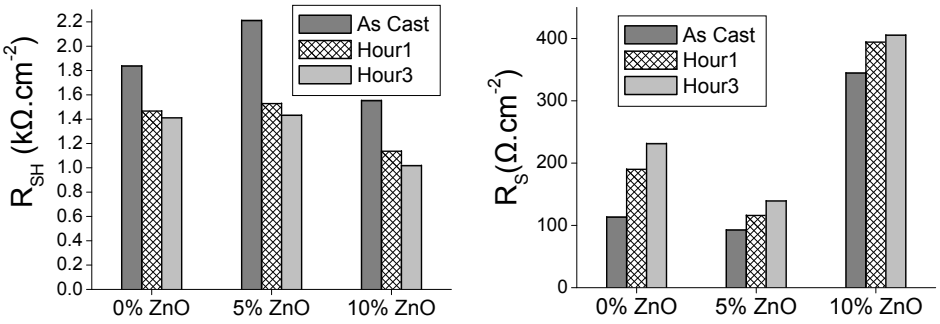

(a) Shunt Resistance

(b) Series Resistance

Figure 5.6: Effect of accelerated aging on shunt and series resistances. Ideally, $R_s = 0$ and $R_{sh} \to \infty$. ZnO addition improves initial series and shunt resistances, and results in a smaller decline in R_s in comparison to devices without ZnO.

As seen in Figure 5.6, the series resistance of the 5%-ZnO devices is lower than that of the 0%-ZnO devices. Additionally, the 5%-ZnO devices show a smaller change in series increases with annealing in comparison to 0%-ZnO devices. This implies that ZnO addition improves not only series resistance, but also stability. While the series resistance of 0%-ZnO devices increases by more than 200%, R_s of 5%- and 10%-ZnO devices increases by only 50% and 17% respectively after 3 hours of annealing.

5.3.3 Electron and Hole Mobilities

In order to further study the effect of ZnO nanoparticles on the charge transport properties, electron-only and hole-only devices are examined. Effective charge mobilities for the devices with ZnO (5%) and without ZnO are extracted using the space charge limited current (SCLC) model with traps. This model is described in detail in Section 4.1. The effective mobility representation is advantageous as it provides a standard formalism for comparison of mobility in disordered semiconductors. Kymakis et al. [75] have proposed that effective mobilities of a polymer film containing carbon nanotubes can be extracted as means of carrier transport comparison. Their work shows that the extracted effective mobilities of the polymer films containing single walled carbon nanotubes are in accordance with experimental data. The extracted electron and hole effective mobilities are plotted in Figure 5.7 as a function of annealing time.

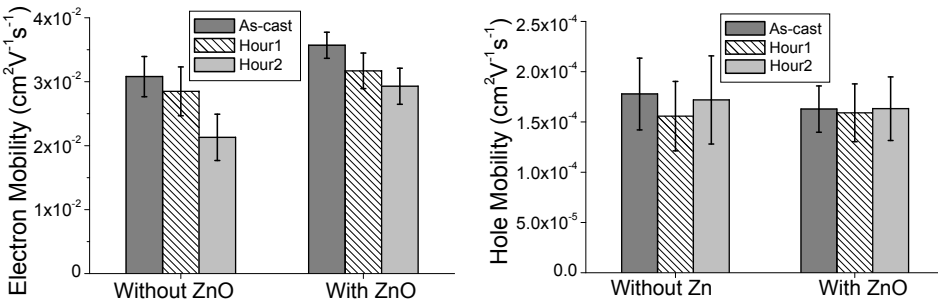

(a) Electron mobility with annealing time (b) Hole mobility with annealing time

Figure 5.7: Effect of accelerated aging on electron and hole effective mobility: adding ZnO nanoparticles not only increases the electron mobility, but also suppresses its degradation with annealing time. Hole mobility is not changed by adding ZnO or annealing

As seen in this figure, adding ZnO improves electron mobility, and the hole mobility remains the same. The improved effective electron mobility can be attributed to the parallel conduction through ZnO nanoparticles which posses higher electron mobilities that are several orders of magnitude higher than the typical mobilities found in organic semiconductors [43, 85].

In addition to exhibiting lower initial mobilities, devices without ZnO also experience steeper declines in electron mobility. The comparative stability of the electron mobility in devices containing ZnO may be responsible for the overall stability of the devices. The small decline in electron mobilities can be examined by studying the morphologies of the D/A networks, and is described in Section 5.4. In this section, it is shown in detail that the change in morphology for devices with and without ZnO is similar; and therefore, the suppression of phase segregation is not the underlying mechanisms for the overall stability. The stability of electron mobility may be due to the stability of ZnO nanoparticles. ZnO nanoparticles continue transporting electrons as the P3HT and PCBM phase segregation takes place and PCBM crystals forms. For more information on the morphology, please refer to Section 5.4.

5.3.4 Trap Density

As mentioned in Section 4.1, the power parameter α in Equation 4.5 relates trap density to the power-law behavior, and is a powerful tool in examining the underlying aging mechanisms. This is a semi-quantitative method which can be roughly used to investigate the density of trapped states, and suggests that current is proportional to the width of the exponential tail, E_b, which is as a measure of trap density (see Figure 4.2). These principles can be used to extract the contribution of ZnO to the total trap density, and the effect on conduction. As previously described, α can be extracted by using the slope of the J/g versus V, and is shown in Figure 5.8. The values for α shown in this figure suggest that introduction of ZnO does not significantly change the shape of the the exponentially tail or the trap density affecting electrons or holes.

5.4 Morphology

This section examines the film and particle morphology in an effort to show the effect of annealing on devices with and without ZnO. Figure 5.9 shows

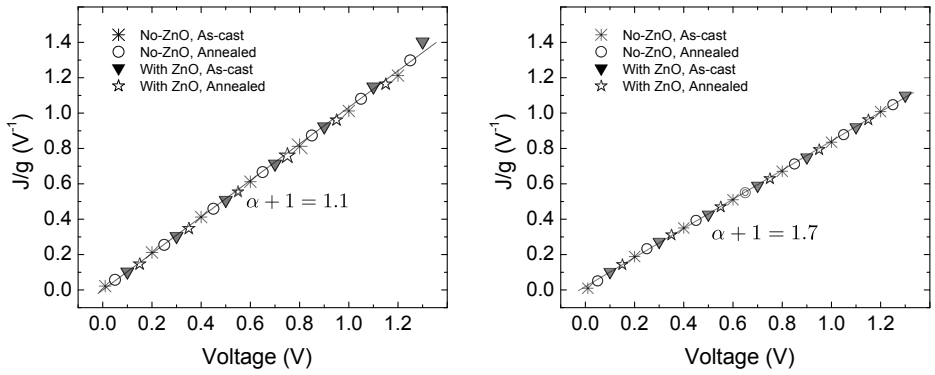

(a) Holes (b) Electrons

Figure 5.8: α extraction for 0% and 5% ZnO devices: J/g vs. V characteristics of electron-only devices, before and after annealing for 2 hours: the slope gives values for α, and an increase in α corresponds to an increase in the trap density

the ZnO particles captured by transmission electron microscopy (TEM). The particle seems to be composed of a lump of several smaller particles in the order of tens of nanometer. This may be because high surface tension of very small inorganic nanocrystals makes them unstable, and thus they have a tendency to grow to larger particles by a process called "Ostwald ripening" [41].

As discussed in Section 3, the TEM samples were prepared by dispensing a drop of ZnO in DCB on a copper mesh grid sample and, therefore, it may be possible that the drying of DCB in fact encourages the aggregation of the ZnO. The ZnO particles may be more evenly dispersed in the P3HT:PCBM film than shown, and further evidence is required for conclusive results.

The morphology of P3HT:PCBM is examined by TEM images. The binary network of P3HT and PCBM can be observed in Figure 5.10, before and after thermal annealing. The higher electron density of P3HT compared with PCBM cause electrons to be scattered more efficiently, thus, the darker regions in the TEM images are regions of phase-separated P3HT. In the TEM images of the as-cast samples, the morphology is well developed and

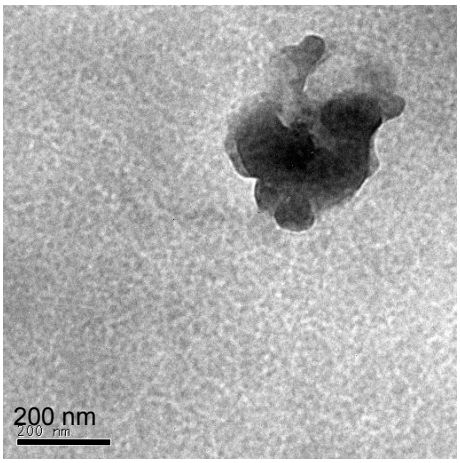

Figure 5.9: TEM images of zinc oxide nanoparticles.

the donor and acceptor domains show a typical feature size of 10-20nm. After thermal annealing and adding ZnO, the domain sizes are practically the same.

Thermal annealing, however, induces the formation of many needle shaped PCBM crystals in the order of several tens of micrometer in length, which are shown in the smaller frames in Figure 5.10(c) and (d). These needle-like formations can better be observed with the optical microscope, and are shown in Figure 5.11. The crystal formations in effect decrease the total D/A interface [86], which may explain the observed drop in J_{sc} with annealing. Similar to the TEM images, the morphology for the annealed devices with and without ZnO remains practically the same, indicating that the observed stability may not be due to phase stability, despite the reports that planting nanoparticles in the films may slow phase segregation [87].

Using the optical microscope, disjointed islands of P3HT-PCBM can be observed for the 10%-ZNO devices, as seen in Figure 5.12. These disjointed islands of film are in the order of several microns. This may explain the decline in performance with increasing ZnO addition from 5 to 10%, as seen in Figure 5.2. The decline is mostly observed in J_{sc}, and the $J-V$ characteristics retains its general shape: short circuit current falls by

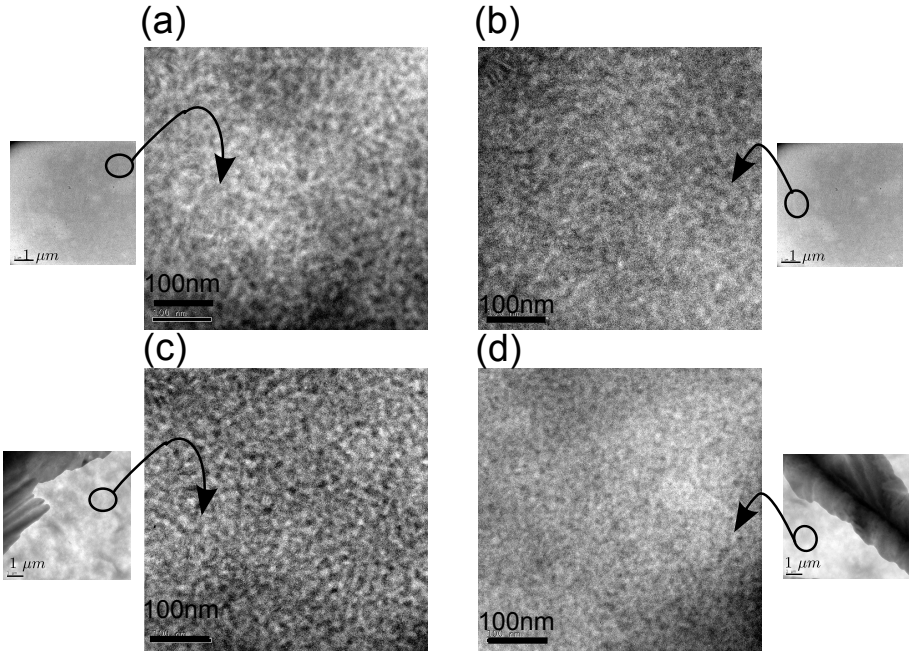

Figure 5.10: TEM images of 0% and 10% devices before and after annealing: (a) As-cast, no-ZnO (b) As-cast, high-ZnO, (c) Annealed, no-ZnO, (d) Annealed, high-ZnO.

around 40% while the fill factor falls by only 15%. This can be explained by studying the morphology of the films. As seen in Figure 5.12, the 10% ZnO films are no longer smooth and consistent, and instead islands of film separated by micro-scale cracks form on the surface. The edges of these disparate film segments may result in imperfections where recombination takes place, essentially deceasing current. Moreover, the formation of these cracks may effectively decrease the total active area, resulting in a decrease in performance. The latter may explain the general retainment of the $I-V$ shape and fill factor of these devices despite the significantly lower J_{sc}.

One possible reason for the formation of these islands may be the interactions between the hydrophobic surface of P3HT:PCBM film [88] and hydrophillic ZnO. It has been shown that varying degrees of surface hydrophilicity contributes to varying polymer accumulation [84, 89]. Addition

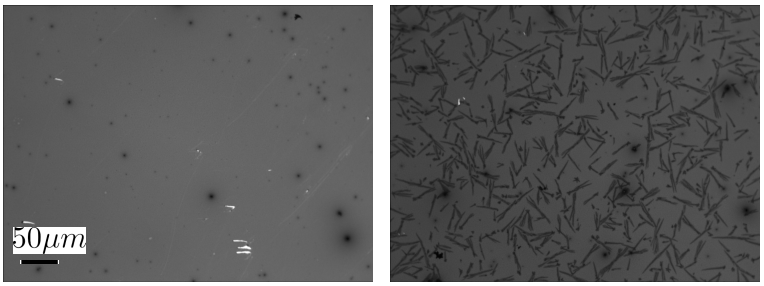

Figure 5.11: Optical micrographs of the P3HT:PCBM films (a) before and (b) after annealing for 2 hours: the formation of the needle-like PCBM clusters was similar for devices with and without ZnO nanoparticles

of ZnO may cause spatial changes of surface energy and charge transfer of the film. If the concentration of ZnO particles becomes high enough, formation of the film may become more favorable on certain areas of the film.

5.5 Electrode Interface

Figure 5.1 shows a small decrease in the open circuit voltage, which was consistently observed for all the tested devices containing ZnO. Moreover, there is a slight s-shape to the $I - V$ curve for the 10%-ZnO devices. This s-shape becomes more pronounced with annealing, as seen in Figure 5.13.

Kumar et al. [40] have proposed that this anomalous feature is due to the presence of strong interface dipoles, which are reported to reduce V_{oc}. Interfacial dipoles, defects, and traps generated as a result of ZnO addition can create barriers for carrier extraction leading to the s-shaped current-voltage graph, and reduce V_{oc}. These defects and traps may become more pronounced with increasing ZnO concentration past an optimal point as well as aging, as showcased in the more pronounced s-shape of the graph.

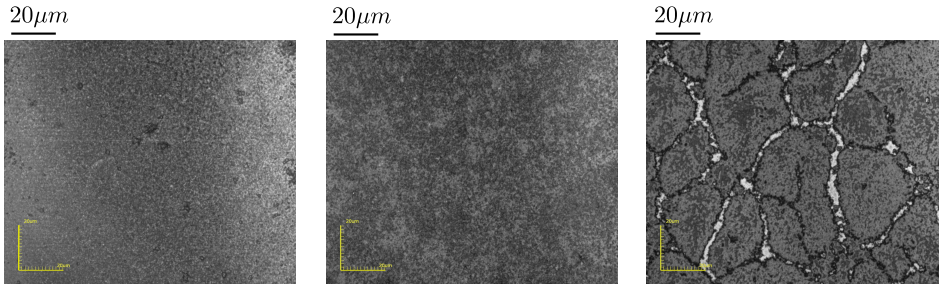

(a) 0%-ZnO (b) 5%-ZnO (c) 10%-ZnO

Figure 5.12: Microscopic morphology change with the addition of ZnO nanoparticle: while the samples containing no-ZnO and 5%-ZnO remain consistent, islands of film seperated by micro-scale cracks form on the 10%-ZnO films

5.6 Areas for Improvement

The following recommendations can be implemented as a part of future work:

Reduce nanoparticle size: for this project, the nanoparticles used are less than 220 nm, which is on the same order as the P3HT:PCBM film thickness. In order to maximize ZnO-polymer surface area, it is suggested to fabricate smaller nanoparticles. Some evidence exists that smaller nanoparticles may improve the performance by a larger extent than it was observed in this project [43]. Moreover, decreasing the nanoparticles size may stabilize the phase segregation, and induce stability [87].

Increase nanoparticle size uniformity: the nanoparticles used for this project ranged from tens of nm to 200nm, with a wide and unknown dispersion. In order to properly study the effect of nanoparticles, it is suggested to use a finer and more controlled particle dispersion.

Use weight percentage as a measure of ZnO concentration: because the ZnO nanoparticles are filtered out from a wet solution, there is no reliable method for measuring the weight of ZnO, and therefore, solution vol% was used as means of keeping track of ZnO concentration. Knowing the exact amount of ZnO in wt% will improve the confidence and the repeatability

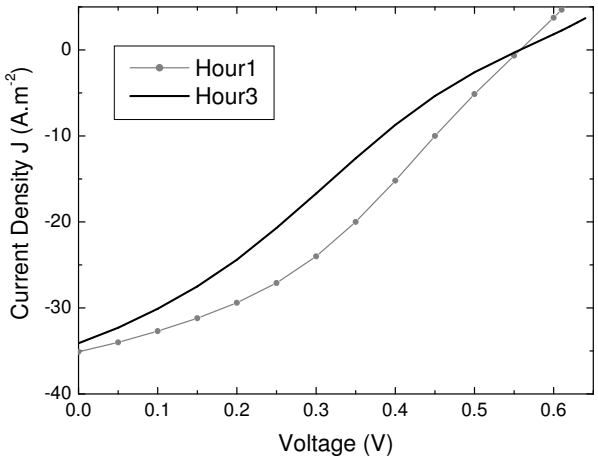

Figure 5.13: S-shaped $J - V$ curves of 10%-ZnO devices, with subsequent change with annealing

of the results. Currently, in order to acquire more accurate concentration measurements, X-ray diffuse scattering (XDS) tests are being carried out. This test can be used to analyze the amount of each material in the films, and get an understanding of what fraction involves ZnO.

Use surfactants: high surface tension of very small nanocrystals makes them unstable, and thus the ZnO nanoparticles show a tendency to grow to larger particles, as seen in Figure 5.9. The use of surfactants can prevent the aggregation of the nanoparticles, and improve the solution/dispersion characteristics of the particles in the polymer matrices [41]. The use of surfactant, however, can change the the optical and physical properties of ZnO nanoparticles [90, 91]. The change in ZnO properties upon surfactant addition must therefore be taken into consideration.

5.7 Conclusion

In the quest for stable, efficient, low-cost polymer solar cells, the pressure is often on the power conversion efficiency, and other equally important

areas of research, such as stability, are often neglected. While the use of ZnO in organic solar cells has been reported to improve power conversion, the degradation mechanisms have not been studied in much depth. In this chapter, the effect of doping P3HT:PCBM solar cells with ZnO nanoparticles is examined on efficiency and stability of these devices.

It is observed that adding small amounts of ZnO can increase both the efficiency and stability of the PVs. The observed improvements, however, are a function of concentration; while the 5%-ZnO devices seem to experience improvements in photoinduced current, fill factor, efficiency and stability, addition of further ZnO results in a loss of power conversion. This is attributed to the formation of cracks on the surface of the active area films. For the 0, and 5% devices, the morphology of the films shows no difference between the samples with and without ZnO for as-cast and annealed devices.

ZnO-P3HT:PCBM cells do not seem to differ in incident light absorption. By using an expanded *pn* junction concept, photovoltaic parameters are extracted. The ideality factor for the devices increased with ZnO addition, implying recombination increases between ZnO and the polymer film. The phase segregation of the D/A with time also seems to contribute to the ideality factor. Saturation current and shunt resistance improve upon 5% ZnO addition; this may suggest that ZnO demonstrates hole blocking properties. Most importantly, conductivity not only improves with ZnO addition, but also experiences a slower rate of decline with annealing time. The extracted effective electron mobilities for 5%-ZnO devices are improved and show comparative stability. The hole mobilities do not change with ZnO addition or annealing. It is concluded that the stability of electron mobilities with aging may be be responsible for the overall stability of hybrid cells.

Chapter 6

Thesis Summary and Future Work

One of the major problems with organic solar cells is low charge mobilities, and therefore, some research effort has been focused on improving the transport properties. Conduction in organic films depends on the morphology, polymer phase segregation, and degree of polymer order. Two mechanisms reported to improve conduction are regioregularity enhancement and ZnO nanoparticles doping. While improvements in performance have been reported, stability has not been quantitatively documented for these devices. The aim of this thesis was to report the effect of RR and ZnO nanoparticles on degradation of organic PVs. Conduction mechanisms in organic materials, however, are not well understood, and are extremely difficult. This is further complicated by the fact that the degree of structural order and conduction strongly depends on the processing conditions. Therefore, semi-compact models that help with understanding and optimizing the performance of organic bulk-heterojunction are extremely valuable. A suitable model takes the effects of disorder and charge trapping as well as recombination processes into account. This thesis aimed to apply such models to gain insight into the mechanisms responsible for the degradation of the devices.

The mobility edge model was used to explore the relation between structural order and electronic conduction in regioregular P3HT:PCBM films as well as P3HT:PCBM films with ZnO nanoparticles. This model provides approximate, yet critical information on the material properties, including density of states, trap generation with annealing, changes in effective mobility with annealing and the effect of disorder-induced localized states on

transport. The use of effective mobility allows the separation of conductivity from device and bias attributes. This model, however, has been applied to this project in a minimal capacity, and has the potential of significantly increasing the understanding of transport properties of organic solar cells. Even though the model captures the essential features of the organic films, more accuracy in modeling the charge transport properties of the devices must be obtained. One method is by introducing a more realistic density of states, which can be determined experimentally. As a part of future work, a suitable theoretical description of the charge transport and recombination processes can also be developed to predict the performance of organic bulk-heterojunction solar cells. Ideally, this model should be capable of reproducing dark and illuminated current-voltage curves. Such a description is currently not available for degradation of organic solar cells. For this model, the major assumption would be that the leading recombination mechanism is the recombination via tail states, which is currently a source of debate [83, 92–94].

The loss mechanisms in BHJ solar cells raise interesting physics questions, and an understanding of these processes is required for the effort to improve solar-cell performance. One model that has been used recently to gain better understanding of these process is the expanded *pn* junction model. This model was used in this thesis to investigate the relationship between fill factor and ZnO concentration as well as aging. This work aimed to systematically investigate the effects of the characteristic properties of the organic layer to the FF, and relate the photovoltaic properties to the morphology characteristics. Recently, Street et al. have used this model in an in depth study of recombination processes in polycarbazole/fullerene blends [83]. Recommended future work includes carrying out similar in depth analysis to find what recombination mechanism is most likely at ZnO-polymer interface. Moreover, the expanded *pn* junction model can be further developed by integrating the voltage-dependance of photocurrent into the equivalent circuit.

Bibliography

[1] A. Moliton and J. Nunzi, "How to model the behaviour of organic photovoltaic cells," *Polymer International*, vol. 55, no. 6, pp. 583–600, 2006.

[2] N. E. B. G. of Canada, "NEB - energy reports - canadas energy future - reference case and scenarios to 2030 - energy market assessment." http://www.neb-one.gc.ca/clf-nsi/rnrgynfmtn/nrgyrprt/nrgyftr/2007/nrgyftr2007-eng.html. Canadas Energy Future - Reference Case and Scenarios to 2030 - Energy Market Assessment.

[3] M. I. Hoffert, K. Caldeira, G. Benford, D. R. Criswell, C. Green, H. Herzog, A. K. Jain, H. S. Kheshgi, K. S. Lackner, J. S. Lewis, H. D. Lightfoot, W. Manheimer, J. C. Mankins, M. E. Mauel, L. J. Perkins, M. E. Schlesinger, T. Volk, and T. M. L. Wigley, "Advanced technology paths to global climate stability: Energy for a greenhouse planet," *Science*, vol. 298, pp. 981 –987, Nov. 2002.

[4] S. Pacala and R. Socolow, "Stabilization wedges: Solving the climate problem for the next 50 years with current technologies," *Science*, vol. 305, no. 5686, pp. 968 –972, 2004.

[5] V. Fthenakis, J. E. Mason, and K. Zweibel, "The technical, geographical, and economic feasibility for solar energy to supply the energy needs of the US," *Energy Policy*, vol. 37, pp. 387–399, Feb. 2009.

[6] M. Z. Jacobson, "Review of solutions to global warming, air pollution, and energy security," *Energy & Environmental Science*, vol. 2, no. 2, p. 148, 2009.

[7] S. Beaupré, P. T. Boudreault, and M. Leclerc, "Solar-Energy production and Energy-Efficient lighting: Photovoltaic devices and White-Light-Emitting diodes using poly(2,7-fluorene), poly(2,7-carbazole), and poly(2,7-dibenzosilole) derivatives," *Advanced Materials*, vol. 22, no. 8, pp. E6–E27, 2010.

[8] CanmetENERGY and N. R. C. G. of Canada, "Natural resources canada's CanmetENERGY | leadership in ecoInnovation other photovoltaic support in canada." http://canmetenergy-canmetenergie.nrcan-rncan.gc.ca/eng/renewables/standalone_pv/publications/resume/pv_development.html.

[9] Y. Liang, Z. Xu, J. Xia, S. Tsai, Y. Wu, G. Li, C. Ray, and L. Yu, "For the bright Future-Bulk heterojunction polymer solar cells with power conversion efficiency of 7.4%," *Advanced Materials*, vol. 22, no. 20, pp. E135–E138, 2010.

[10] M. A. Green, K. Emery, Y. Hishikawa, and W. Warta, "Solar cell efficiency tables (version 37)," *Progress in Photovoltaics: Research and Applications*, vol. 19, no. 1, pp. 84–92, 2011.

[11] G. Chidichimo and L. Filippelli, "Organic solar cells: Problems and perspectives," *International Journal of Photoenergy*, vol. 2010, pp. 1–12, 2010.

[12] F. C. Krebs, "Fabrication and processing of polymer solar cells: A review of printing and coating techniques," *Solar Energy Materials and Solar Cells*, vol. 93, pp. 394–412, Apr. 2009.

[13] Y. Kim, S. Cook, S. M. Tuladhar, S. A. Choulis, J. Nelson, J. R. Durrant, D. D. C. Bradley, M. Giles, I. McCulloch, C. Ha, and M. Ree, "A strong regioregularity effect in self-organizing conjugated polymer films and high-efficiency polythiophene:fullerene solar cells," *Nat Mater*, vol. 5, pp. 197–203, Mar. 2006.

[14] V. Kruefu, E. Peterson, C. Khantha, C. Siriwong, S. Phanichphant, and D. L. Carroll, "Flame-made niobium doped zinc oxide nanoparticles in

bulk heterojunction solar cells," *Applied Physics Letters*, vol. 97, no. 5, p. 053302, 2010.

[15] D. Olson, S. Shaheen, M. White, W. Mitchell, M. vanHest, R. Collins, and D. Ginley, "Band-Offset engineering for enhanced Open-Circuit voltage in PolymerOxide hybrid solar cells," *Advanced Functional Materials*, vol. 17, no. 2, pp. 264–269, 2007.

[16] W. U. Huynh, J. J. Dittmer, and A. P. Alivisatos, "Hybrid Nanorod-Polymer solar cells," *Science*, vol. 295, pp. 2425 –2427, Mar. 2002.

[17] K. Kim, B. Jung, J. Kim, and W. Kim, "Effects of embedding non-absorbing nanoparticles in organic photovoltaics on power conversion efficiency," *Solar Energy Materials and Solar Cells*, vol. 94, pp. 1835–1839, Oct. 2010.

[18] M. O. Reese, A. J. Morfa, M. S. White, N. Kopidakis, S. E. Shaheen, G. Rumbles, and D. S. Ginley, "Pathways for the degradation of organic photovoltaic P3HT:PCBM based devices," *Solar Energy Materials and Solar Cells*, vol. 92, pp. 746–752, July 2008.

[19] A. Salleo, T. W. Chen, A. R. Vlkel, Y. Wu, P. Liu, B. S. Ong, and R. A. Street, "Intrinsic hole mobility and trapping in a regioregular poly(thiophene)," *Physical Review B*, vol. 70, no. 11, p. 115311, 2004.

[20] H. Hoppe and N. Sariciftci, *Polymer Solar Cells*, vol. 214 of *Advances in Polymer Science*. Springer Berlin / Heidelberg, 2008.

[21] M. Kertesz, "Structure and electronic structure of low-band-gap ladder polymers," *Macromolecules*, vol. 28, no. 5, pp. 1475–1480, 1995.

[22] S. Karg, W. Riess, V. Dyakonov, and M. Schwoerer, "Electrical and optical characterization of poly(phenylene-vinylene) light emitting diodes," *Synthetic Metals*, vol. 54, pp. 427–433, Mar. 1993.

[23] G. Yu, J. Gao, J. C. Hummelen, F. Wudl, and A. J. Heeger, "Polymer photovoltaic cells: Enhanced efficiencies via a network of internal

Donor-Acceptor heterojunctions," *Science*, vol. 270, pp. 1789 –1791, Dec. 1995.

[24] J. J. M. Halls, C. A. Walsh, N. C. Greenham, E. A. Marseglia, R. H. Friend, S. C. Moratti, and A. B. Holmes, "Efficient photodiodes from interpenetrating polymer networks," *Nature*, vol. 376, no. 6540, pp. 498–500, 1995.

[25] K. Pichler, R. H. Friend, S. C. Moratti, A. B. Holmes, and J. J. M. Halls, "Exciton diffusion and dissociation in a poly(p-phenylenevinylene)/C60 heterojunction photovoltaic cell," *Applied Physics Letters*, vol. 68, no. 22, pp. 3120–3122.

[26] T. J. Savenije, J. M. Warman, and A. Goossens, "Visible light sensitisation of titanium dioxide using a phenylene vinylene polymer," *Chemical Physics Letters*, vol. 287, pp. 148–153, Apr. 1998.

[27] L. A. A. Pettersson, L. S. Roman, and O. Ingans, "Modeling photocurrent action spectra of photovoltaic devices based on organic thin films," *Journal of Applied Physics*, vol. 86, no. 1, p. 487, 1999.

[28] M. Chandross, S. Mazumdar, S. Jeglinski, X. Wei, Z. V. Vardeny, E. W. Kwock, and T. M. Miller, "Excitons in poly(para-phenylenevinylene)," *Physical Review B*, vol. 50, p. 14702, Nov. 1994.

[29] M. Knupfer, "Exciton binding energies in organic semiconductors," *Applied Physics A: Materials Science & Processing*, vol. 77, no. 5, pp. 623–626, 2003.

[30] J. Nelson, J. J. Kwiatkowski, J. Kirkpatrick, and J. M. Frost, "Modeling charge transport in organic photovoltaic materials," *Accounts of Chemical Research*, vol. 42, pp. 1768–1778, Nov. 2009.

[31] M. C. J. M. Vissenberg and M. Matters, "Theory of the field-effect mobility in amorphous organic transistors," *Physical Review B*, vol. 57, p. 12964, May 1998.

[32] F. Schauer, "Space-charge-limited currents for organic solar cells optimisation," *Solar Energy Materials and Solar Cells*, vol. 87, pp. 235–250, May 2005.

[33] R. A. Street, J. E. Northrup, and A. Salleo, "Transport in polycrystalline polymer thin-film transistors," *Physical Review B*, vol. 71, p. 165202, Apr. 2005.

[34] R. A. Street, "Carrier mobility, structural order, and solar cell efficiency of organic heterojunction devices," *Applied Physics Letters*, vol. 93, no. 13, p. 133308, 2008.

[35] V. Kumar, S. C. Jain, A. K. Kapoor, J. Poortmans, and R. Mertens, "Trap density in conducting organic semiconductors determined from temperature dependence of J-V characteristics," *Journal of Applied Physics*, vol. 94, no. 2, p. 1283, 2003.

[36] C. J. Brabec, A. Cravino, D. Meissner, N. S. Sariciftci, T. Fromherz, M. T. Rispens, L. Sanchez, and J. C. Hummelen, "Origin of the open circuit voltage of plastic solar cells," *Advanced Functional Materials*, vol. 11, no. 5, pp. 374–380, 2001.

[37] D. Rauh, A. Wagenpfahl, C. Deibel, and V. Dyakonov, "Relation of open circuit voltage to charge carrier density in organic bulk heterojunction solar cells," *Applied Physics Letters*, vol. 98, no. 13, p. 133301, 2011.

[38] V. D. Mihailetchi, P. W. M. Blom, J. C. Hummelen, and M. T. Rispens, "Cathode dependence of the open-circuit voltage of polymer:fullerene bulk heterojunction solar cells," *Journal of Applied Physics*, vol. 94, no. 10, p. 6849, 2003.

[39] I. Campbell, S. Rubin, T. Zawodzinski, J. Kress, R. Martin, D. Smith, N. Barashkov, and J. Ferraris, "Controlling schottky energy barriers in organic electronic devices using self-assembled monolayers," *Physical Review B*, vol. 54, no. 20, pp. R14321–R14324, 1996.

[40] A. Kumar, S. Sista, and Y. Yang, "Dipole induced anomalous s-shape I-V curves in polymer solar cells," *Journal of Applied Physics*, vol. 105, no. 9, p. 094512, 2009.

[41] S. Gnes, H. Neugebauer, and N. S. Sariciftci, "Conjugated polymer-based organic solar cells," *Chemical Reviews*, vol. 107, pp. 1324–1338, Apr. 2007. PMID: 17428026.

[42] J. Poortmans and V. Arkhipov, *Thin film solar cells: fabrication, characterization and applications*. John Wiley and Sons, Nov. 2006.

[43] W. Beek, M. Wienk, and R. Janssen, "Efficient hybrid solar cells from zinc oxide nanoparticles and a conjugated polymer," *Advanced Materials*, vol. 16, no. 12, pp. 1009–1013, 2004.

[44] W. J. E. Beek, L. H. Slooff, M. M. Wienk, J. M. Kroon, and R. A. J. Janssen, "Hybrid solar cells using a zinc oxide precursor and a conjugated polymer," *Advanced Functional Materials*, vol. 15, no. 10, pp. 1703–1707, 2005.

[45] S. K. Hau, H. Yip, N. S. Baek, J. Zou, K. OMalley, and A. K. Jen, "Air-stable inverted flexible polymer solar cells using zinc oxide nanoparticles as an electron selective layer," *Applied Physics Letters*, vol. 92, no. 25, p. 253301, 2008.

[46] S. A. Jenekhe and S. Yi, "Efficient photovoltaic cells from semiconducting polymer heterojunctions," *Applied Physics Letters*, vol. 77, p. 2635, Oct. 2000.

[47] S. van Bavel, E. Sourty, G. de With, K. Frolic, and J. Loos, "Relation between photoactive layer thickness, 3D morphology, and device performance in P3HT/PCBM Bulk-Heterojunction solar cells," *Macromolecules*, vol. 42, pp. 7396–7403, Oct. 2009.

[48] M. Reyes-Reyes, K. Kim, J. Dewald, R. Lpez-Sandoval, A. Avadhanula, S. Curran, and D. L. Carroll, "Meso-Structure formation for enhanced

organic photovoltaic cells," *Organic Letters*, vol. 7, pp. 5749–5752, Dec. 2005.

[49] W. Ma, C. Yang, X. Gong, K. Lee, and A. Heeger, "Thermally stable, efficient polymer solar cells with nanoscale control of the interpenetrating network morphology," *Advanced Functional Materials*, vol. 15, no. 10, pp. 1617–1622, 2005.

[50] K. Kawano, J. Sakai, M. Yahiro, and C. Adachi, "Effect of solvent on fabrication of active layers in organic solar cells based on poly(3-hexylthiophene) and fullerene derivatives," *Solar Energy Materials and Solar Cells*, vol. 93, pp. 514–518, Apr. 2009.

[51] S. E. Shaheen, C. J. Brabec, N. S. Sariciftci, F. Padinger, T. Fromherz, and J. C. Hummelen, "2.5% efficient organic plastic solar cells," *Applied Physics Letters*, vol. 78, no. 6, p. 841, 2001.

[52] S. Jin, B. V. K. Naidu, H. Jeon, S. Park, J. Park, S. C. Kim, J. W. Lee, and Y. Gal, "Optimization of process parameters for high-efficiency polymer photovoltaic devices based on P3HT:PCBM system," *Solar Energy Materials and Solar Cells*, vol. 91, pp. 1187–1193, Aug. 2007.

[53] V. D. Mihailetchi, H. Xie, B. de Boer, L. M. Popescu, J. C. Hummelen, P. W. M. Blom, and L. J. A. Koster, "Origin of the enhanced performance in poly(3-hexylthiophene): [6,6]-phenyl c[sub 61]-butyric acid methyl ester solar cells upon slow drying of the active layer," *Applied Physics Letters*, vol. 89, no. 1, p. 012107, 2006.

[54] T. Martens, "Morphology of MDMO-PPV:PCBM bulk heterojunction organic solar cells studied by AFM, KFM, and TEM," in *Proceedings of SPIE*, (Seattle, WA, USA), pp. 40–47, 2003.

[55] X. Yang, J. Loos, S. C. Veenstra, W. J. H. Verhees, M. M. Wienk, J. M. Kroon, M. A. J. Michels, and R. A. J. Janssen, "Nanoscale morphology of High-Performance polymer solar cells," *Nano Letters*, vol. 5, pp. 579–583, Apr. 2005.

[56] D. Chirvase, J. Parisi, J. C. Hummelen, and V. Dyakonov, "Influence of nanomorphology on the photovoltaic action of polymerfullerene composites," *Nanotechnology*, vol. 15, no. 9, pp. 1317–1323, 2004.

[57] J. M. Kroon, M. M. Wienk, W. J. H. Verhees, and J. C. Hummelen, "Accurate efficiency determination and stability studies of conjugated polymer/fullerene solar cells," *Thin Solid Films*, vol. 403-404, pp. 223–228, Feb. 2002.

[58] H. Neugebauer, C. Brabec, J. C. Hummelen, and N. S. Sariciftci, "Stability and photodegradation mechanisms of conjugated polymer/fullerene plastic solar cells," *Solar Energy Materials and Solar Cells*, vol. 61, pp. 35–42, Feb. 2000.

[59] M. Yahiro, D. Zou, and T. Tsutsui, "Recoverable degradation phenomena of quantum efficiency in organic EL devices," *Synthetic Metals*, vol. 111-112, pp. 245–247, June 2000.

[60] E. Gautier-Thianche, "Electrode interface effects on ITO/polymer/metal light emitting diodes," in *Proceedings of SPIE*, (San Jose, CA, USA), pp. 104–107, 1997.

[61] Y. Sahin, S. Alem, R. de Bettignies, and J. Nunzi, "Development of air stable polymer solar cells using an inverted gold on top anode structure," *Thin Solid Films*, vol. 476, pp. 340–343, Apr. 2005.

[62] C. Chang and S. Chen, "Effect of ionization potential change in poly(3,4-ethylenedioxythiophene):poly(styrenesulfonic acid) on the performance of polymer light emitting diodes due to its reaction with indium tin oxide," *Applied Physics Letters*, vol. 91, no. 10, p. 103514, 2007.

[63] T. M. Clarke, A. M. Ballantyne, J. Nelson, D. D. C. Bradley, and J. R. Durrant, "Free energy control of charge photogeneration in Polythiophene/Fullerene solar cells: The influence of thermal annealing on P3HT/PCBM blends," *Advanced Functional Materials*, vol. 18, no. 24, pp. 4029–4035, 2008.

[64] S. Ebadian, B. Gholamkhass, S. Shambayati, S. Holdcroft, and P. Servati, "Effects of annealing and degradation on regioregular polythiophene-based bulk heterojunction organic photovoltaic devices," *Solar Energy Materials and Solar Cells*, vol. 94, pp. 2258–2264, Dec. 2010.

[65] S. Shambayati, B. Gholamkhass, S. Ebadian, S. Holdcroft, and P. Servati, "Modeling the effect of annealing and regioregularity on electron and hole transport characteristics of bulk heterojunction organic photovoltaic devices," *MRS Online Proceedings Library*, vol. 1270, p. null, 2010.

[66] D. L. Pulfrey, *Understanding Modern Transistors and Diodes*. Cambridge University Press, 1 ed., Mar. 2010.

[67] M. Jörgensen, K. Norrman, and F. C. Krebs, "Stability/degradation of polymer solar cells," *Solar Energy Materials and Solar Cells*, vol. 92, pp. 686–714, July 2008.

[68] R. D. Bettignies, J. Leroy, M. Firon, and C. Sentein, "Accelerated lifetime measurements of P3HT:PCBM solar cells," *Synthetic Metals*, vol. 156, pp. 510–513, Apr. 2006.

[69] Y. Kim, S. A. Choulis, J. Nelson, D. D. C. Bradley, S. Cook, and J. R. Durrant, "Device annealing effect in organic solar cells with blends of regioregular poly(3-hexylthiophene) and soluble fullerene," 2005.

[70] V. Chellappan, G. M. Ng, M. J. Tan, W. Goh, and F. Zhu, "Imbalanced charge mobility in oxygen treated polythiophene/fullerene based bulk heterojunction solar cells," *Applied Physics Letters*, vol. 95, no. 26, p. 263305, 2009.

[71] M. Vogel, J. Strotmann, B. Johnev, M. C. Lux-Steiner, and K. Fostiropoulos, "Influence of nanoscale morphology in small molecule organic solar cells," *Thin Solid Films*, vol. 511-512, pp. 367–370, July 2006.

[72] V. Mihailetchi, H. Xie, B. de Boer, L. Koster, and P. Blom, "Charge transport and photocurrent generation in poly(3-hexylthiophene): Methanofullerene Bulk-Heterojunction solar cells," *Advanced Functional Materials*, vol. 16, no. 5, pp. 699–708, 2006.

[73] K. Sivula, C. K. Luscombe, B. C. Thompson, and J. M. J. Frèchet, "Enhancing the thermal stability of Polythiophene:Fullerene solar cells by decreasing effective polymer regioregularity," *Journal of the American Chemical Society*, vol. 128, pp. 13988–13989, Nov. 2006.

[74] P. Servati, A. Nathan, and G. A. J. Amaratunga, "Generalized transport-band field-effect mobility in disordered organic and inorganic semiconductors," *Physical Review B*, vol. 74, p. 245210, Dec. 2006.

[75] Kymakis, "Effective mobility and photocurrent in carbon nanotube-polymer composite photovoltaic cells," *Nanotechnology*, vol. 18, no. 43, p. 435702, 2007.

[76] M. Gailberger and H. Bssler, "dc and transient photoconductivity of poly(2-phenyl-1,4-phenylenevinylene)," *Physical Review B*, vol. 44, p. 8643, Oct. 1991.

[77] Z. Shen, U. Kortshagen, and S. A. Campbell, "Electrical characterization of amorphous silicon nanoparticles," *Journal of Applied Physics*, 2004.

[78] P. Vanlaeke, A. Swinnen, I. Haeldermans, G. Vanhoyland, T. Aernouts, D. Cheyns, C. Deibel, J. D'Haen, P. Heremans, J. Poortmans, and J. Manca, "P3HT/PCBM bulk heterojunction solar cells: Relation between morphology and electro-optical characteristics," *Solar Energy Materials and Solar Cells*, vol. 90, pp. 2150–2158, Sept. 2006.

[79] D. Sridev and K. V. Rajendran, "Synthesis and optical characteristics of ZnO nanocrystals," *Bulletin of Materials Science*, vol. 32, no. 2, pp. 165–168, 2009.

[80] H. Hoppe, N. Arnold, D. Meissner, and N. S. Sariciftci, "Modeling of optical absorption in conjugated polymer/fullerene bulk-heterojunction plastic solar cells," *Thin Solid Films*, vol. 451-452, pp. 589–592, Mar. 2004.

[81] C. Waldauf, M. C. Scharber, P. Schilinsky, J. A. Hauch, and C. J. Brabec, "Physics of organic bulk heterojunction devices for photovoltaic applications," *Journal of Applied Physics*, vol. 99, p. 4503, May 2006.

[82] J. H. Lee, S. Cho, A. Roy, H. Jung, and A. J. Heeger, "Enhanced diode characteristics of organic solar cells using titanium suboxide electron transport layer," *Applied Physics Letters*, vol. 96, no. 16, p. 163303, 2010.

[83] R. A. Street, M. Schoendorf, A. Roy, and J. H. Lee, "Interface state recombination in organic solar cells," *Physical Review B*, vol. 81, p. 205307, May 2010.

[84] J. Xue, S. Uchida, B. P. Rand, and S. R. Forrest, "4.2% efficient organic photovoltaic cells with low series resistances," *Applied Physics Letters*, vol. 84, no. 16, p. 3013, 2004.

[85] D. C. Olson, J. Piris, R. T. Collins, S. E. Shaheen, and D. S. Ginley, "Hybrid photovoltaic devices of polymer and ZnO nanofiber composites," *Thin Solid Films*, vol. 496, pp. 26–29, Feb. 2006.

[86] K. Sivula, Z. T. Ball, N. Watanabe, and J. M. J. Fréchet, "Amphiphilic diblock copolymer compatibilizers and their effect on the morphology and performance of Polythiophene:Fullerene solar cells," *Advanced Materials*, vol. 18, no. 2, pp. 206–210, 2006.

[87] T. Kietzke, D. Neher, M. Kumke, R. Montenegro, K. Landfester, and U. Scherf, "A nanoparticle approach to control the phase separation in polyfluorene photovoltaic devices," *Macromolecules*, vol. 37, pp. 4882–4890, June 2004.

[88] Q. Dong, Y. Zhou, J. Pei, Z. Liu, Y. Li, S. Yao, J. Zhang, and W. Tian, "All-spin-coating vacuum-free processed semi-transparent inverted polymer solar cells with PEDOT:PSS anode and PAH-D interfacial layer," *Organic Electronics*, vol. 11, pp. 1327–1331, July 2010.

[89] H. Liao, L. Chen, Z. Xu, G. Li, and Y. Yang, "Highly efficient inverted polymer solar cell by low temperature annealing of cs[sub 2]CO[sub 3] interlayer," *Applied Physics Letters*, vol. 92, no. 17, p. 173303, 2008.

[90] H. Usui, "Surfactant concentration dependence of structure and photocatalytic properties of zinc oxide rods prepared using chemical synthesis in aqueous solutions," *Journal of Colloid and Interface Science*, vol. 336, pp. 667–674, Aug. 2009. PMID: 19473665.

[91] B. Shahmoradi, K. Soga, S. Ananda, R. Somashekar, and K. Byrappa, "Modification of neodymium-doped ZnO hybrid nanoparticles under mild hydrothermal conditions," *Nanoscale*, vol. 2, no. 7, p. 1160, 2010.

[92] Z. Z. Zhi, Y. Qi, H. Z. Yang, J. H. Wang, X. M. Yu, and B. S. Zhang, "<title> effects of annealing temperature on optical properties of ZnO nanocrystals embedded in SiO ₂ matrix thin films </title>," *Journal of Physics D: Applied Physics*, vol. 40, no. 14, pp. 4281–4284, 2007.

[93] R. A. Street, "Reply to "Comment on 'Interface state recombination in organic solar cells' "," *Physical Review B*, vol. 82, p. 207302, Nov. 2010.

[94] M. Hilczer and M. Tachiya, "Unified theory of geminate and bulk Electron-Hole recombination in organic solar cells," *The Journal of Physical Chemistry C*, vol. 114, pp. 6808–6813, Apr. 2010.

Appendix A

Regioregularity

P3HT belongs to a class of polymers for which the monomers (3-alkylthiophenes) are asymmetric. Non-regiospecific polymerization can result in three types of structures: Alkylthiophenes may couple head-to-head (HH), head-to-tail (HT) or tail-to-tail (TT) as depicted in Figure A.1. A regioregular P3HT contains HT couplings. This allows the polymer to readily self-assemble and adopt planar conformations both in solution and in the solid state. The highly ordered structure shows strong interchain electronic interaction and electronic delocalization, high hole mobility, improved absorption in the visible region, and a tendency to crystallize into ordered domains [64].

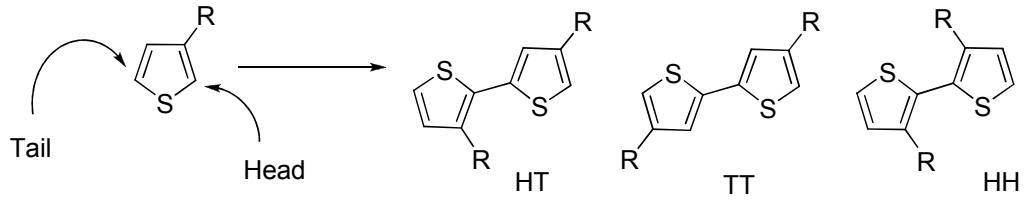

Figure A.1: coupling possibilities of 3-alkylthiophenes, printed with permission from Bob Gholamkhass

Appendix B

Description of the Mobility Edge Model

B.1 Transport in Exponential Tail

The density of carriers excited to the isoelectronic transport band n_{band} is shown in equation B.1 in accordance to Boltzmann's approximation [74], where N_b is the effective state density for the transport band, and E_F is the Fermi Fermi energy that is defined negative with respect to the mobility edge.

$$n_{\text{band}} = N_b \exp\left(\frac{E_F}{kT}\right) \tag{B.1}$$

The density of trapped carriers as a function of Fermi energy is retrieved from the density of states $g(E)$ using equation 4.1,

$$n_{\text{trapped}} = \int_0^{E_b} g(E) f(E, E_F) dE \tag{B.2}$$

where $f(E, E_F)$ is the Fermi-Dirac function:

$$f(E, E_F) = \left(1 + \exp\frac{(E - E_F)}{kT}\right)^{-1} \tag{B.3}$$

Combining equations B.2 and B.3:

$$n_{trapped} = \int_0^{E_G} g(E)f(E,E_F)dE \tag{B.4}$$

$$= N_t \exp(\frac{E_F}{kT_t})u(E_F,T_t,T) \tag{B.5}$$

$$\tag{B.6}$$

Where E_G is the bandgap and $u(E_F,T_t,T)$ is defined as:

$$u(E_F,T_t,T) = \int_{X_{GF}}^{X_F} \frac{dx}{1+x^\alpha} \tag{B.7}$$

In equation 3.3, the bounds for the integral are $X_{GF} = \exp(\frac{E_G-E_F}{kT_t})$ and $X_F = \exp(\frac{-E_F}{kT_t})$. Based on numerical solutions, the integral u in equation B.8 approaches unity at low T, and approaches $\frac{1}{2}\exp(\frac{E_F}{kT_t})$ at high T. For intermediate temperatures, u attains a value between these two extremes. Although this integral is not analytically solvable over all temperatures, one finds that n_{trapped} as a function of E_F has a general exponential characteristic in typical temperature ranges, and thus can be written as

$$n_{\text{trapped}} = N_t' \exp(\frac{E_F}{kT_t'}) \tag{B.8}$$

The values relating N_t and N_t', T_t and T_t' at room temperature are found numerically using the model purposed by Servati et al. [74], and are shown in Figure B.1.

n_{band} and n_{trapped} are related by combining equations B.1 and B.2, where $\alpha' = {}^{T_t'}/_{T}$ [75]. Since $n_{\text{band}} \ll n_{\text{trapped}}$, it can be assumed that total carrier concentration, $n = n_{\text{trapped}} + n_{\text{band}} \approx n_{\text{trapped}}$. This gives:

$$n_{\text{band}} = \theta n^{\frac{T_t'}{T}} \tag{B.9}$$

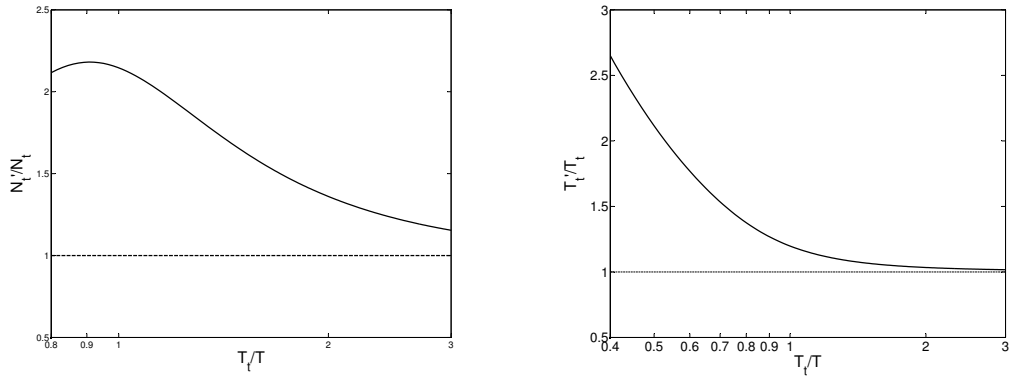

Figure B.1: α extraction, yielding ohmic transport for all devices, regardless of regioregularity or aging

$\theta = {}^{N_b}/_{(N_t')^{\alpha'}}$. This equation has been found to empirically hold for determining the equilibrium between free carrier density and total carrier concentration for many organic semiconductors [39].

B.2 Effective Mobility

The effective mobility can be found according to Figure 4.2. Using a reference point N_0 as reported by [19]., and using Equations B.9, effective mobility at a reference carrier concentration N_0 can be defined as:

$$\mu_{\text{eff}} = \mu_0 \frac{n_{\text{mobile}}}{n_{\text{total}}} = \mu_{\text{band}} \frac{N_b}{N_0} \left(\frac{N_0}{N_t'}\right)^{\frac{T_t'}{T}} \tag{B.10}$$

By replacing Equation B.10 in Equation 4.2, effective mobility can be extracted from measured $J - V$ characteristics:

$$J = q\mu_{eff} N_0 \kappa \left(\frac{\varepsilon}{qN_0}\right)^{\alpha} (V_D - V_t)^{\alpha+1}/t^{2\alpha+1} \tag{B.11}$$

Where N_0 represents effective mobility at a reference carrier concentra-

tion $N_0 = 2 \times 10^{16}$ cm^{-3} [74].

Appendix C

Hole-only, 93% and 98%-RR Dark Currents Measurements

The following figures show the data for all samples, numbered from 1 - 6, for hole only devices, and includes both 93% and 98% RR devices. The first figure shows as is devices, while second and third show devices after being annealed for 1 hour and 2 hours, respectively.

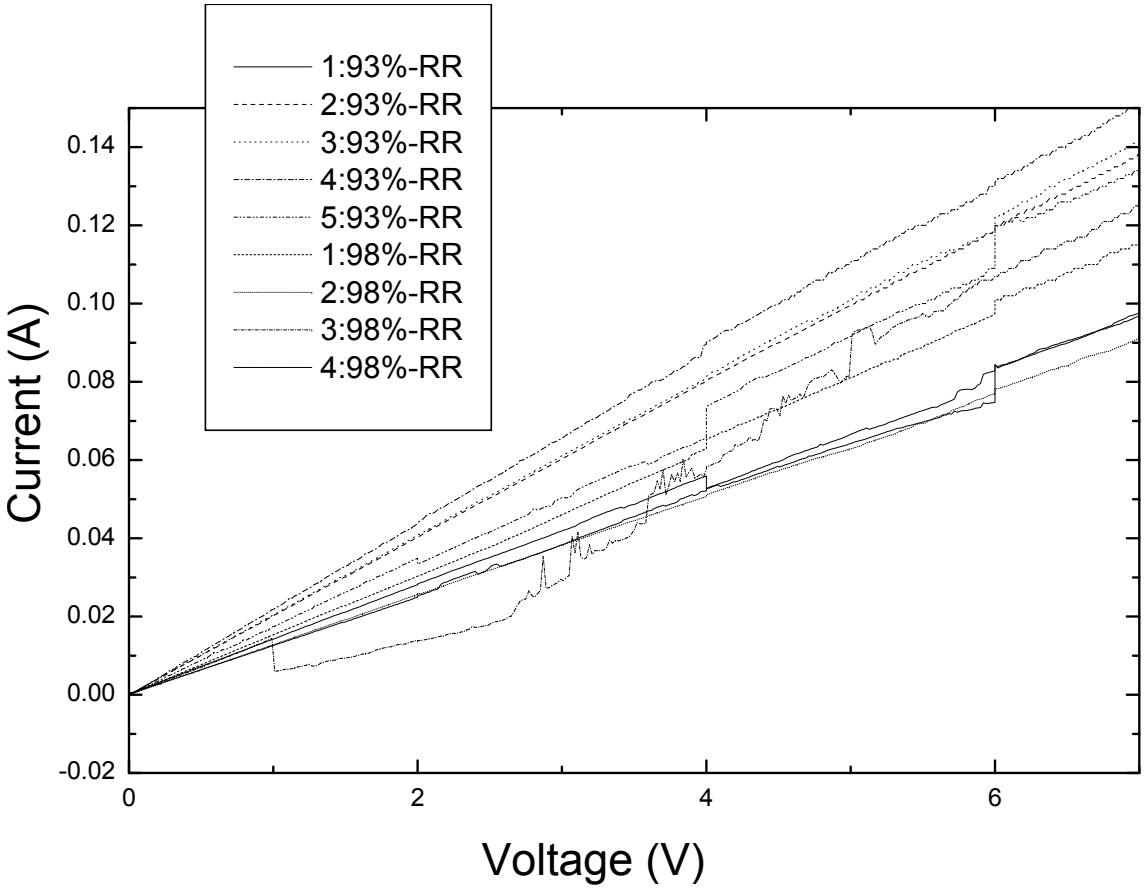

Figure C.1: Hole only, 93% and 98%-RR dark currents - as is devices

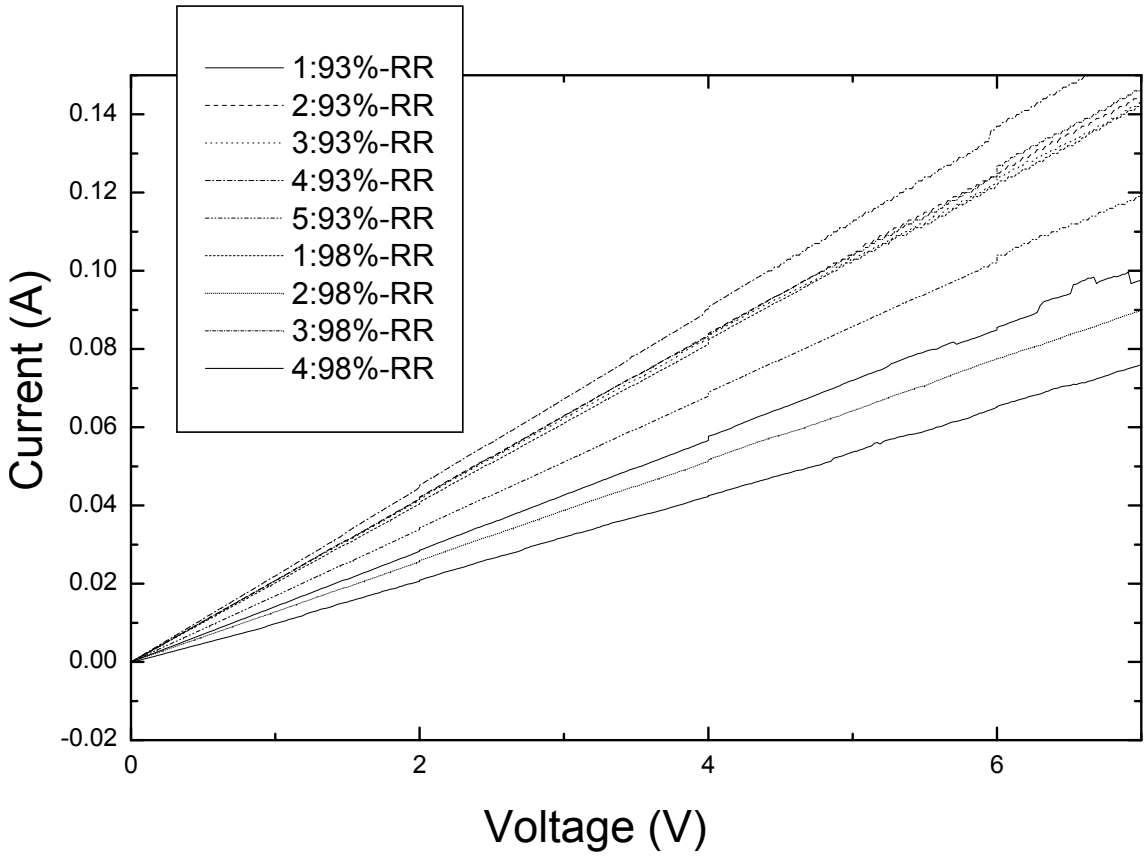

Figure C.2: Hole only, 93% and 98%-RR dark Currents - annealed 1 hour

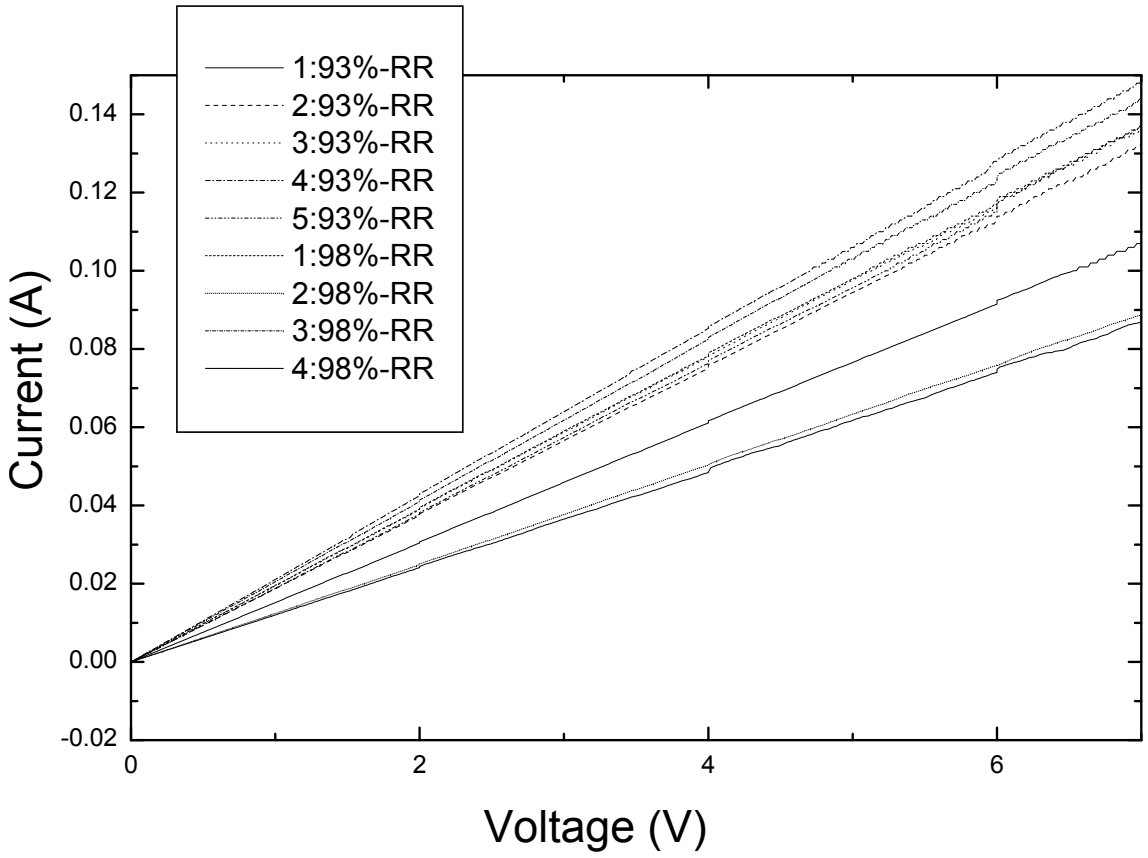

Figure C.3: Hole only, 93% and 98%-RR dark currents - annealed 2 hours

Appendix D

Electron-only, 93% and 98%-RR Dark Current Measurements

The following figures show the data for all samples, numbered from 1 - 6, for electron only devices, and includes both 93% and 98% RR devices. The first figure shows as is devices, while second, third and fourth show devices after being annealed for 1, 2 and 3 hours, respectively.

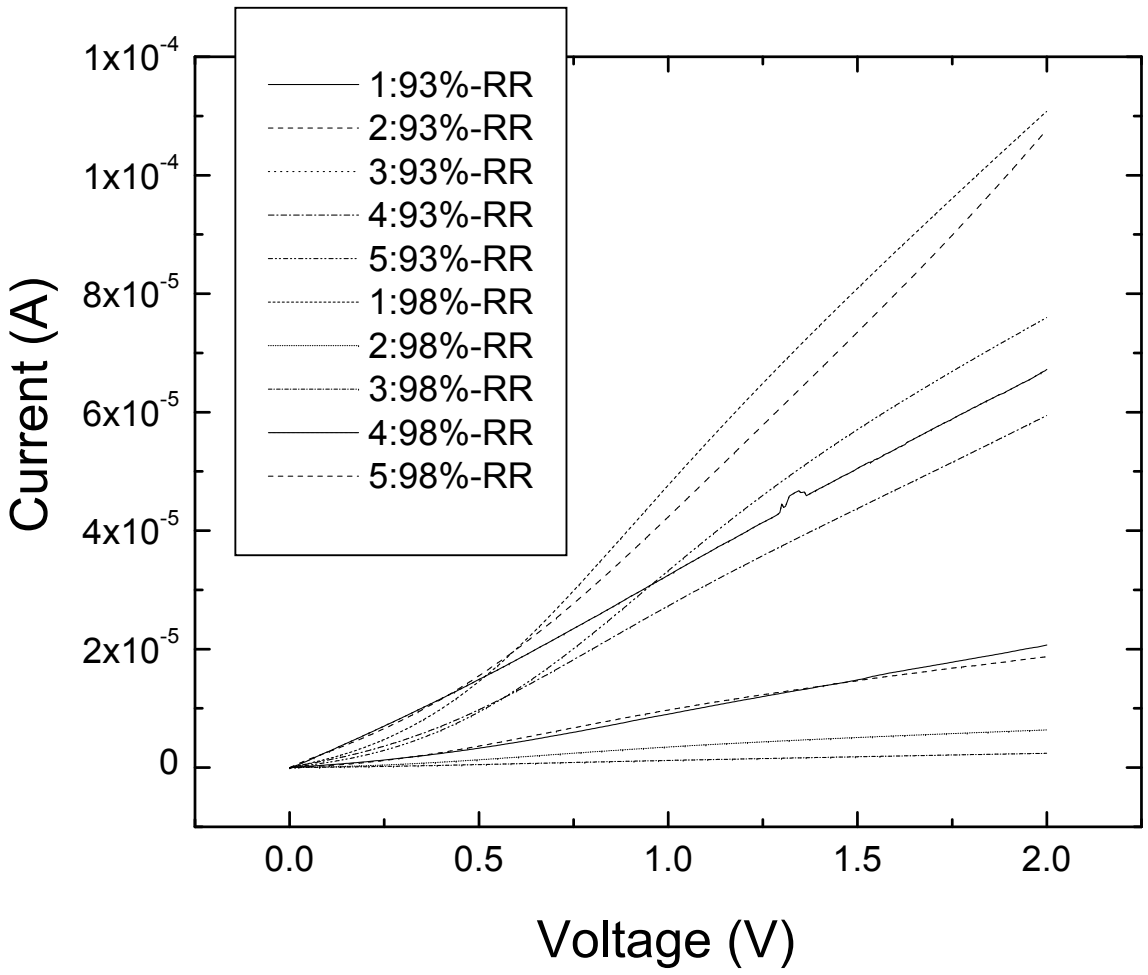

Figure D.1: Electron-only, 93% and 98%-RR dark current measurement of as-cast devices

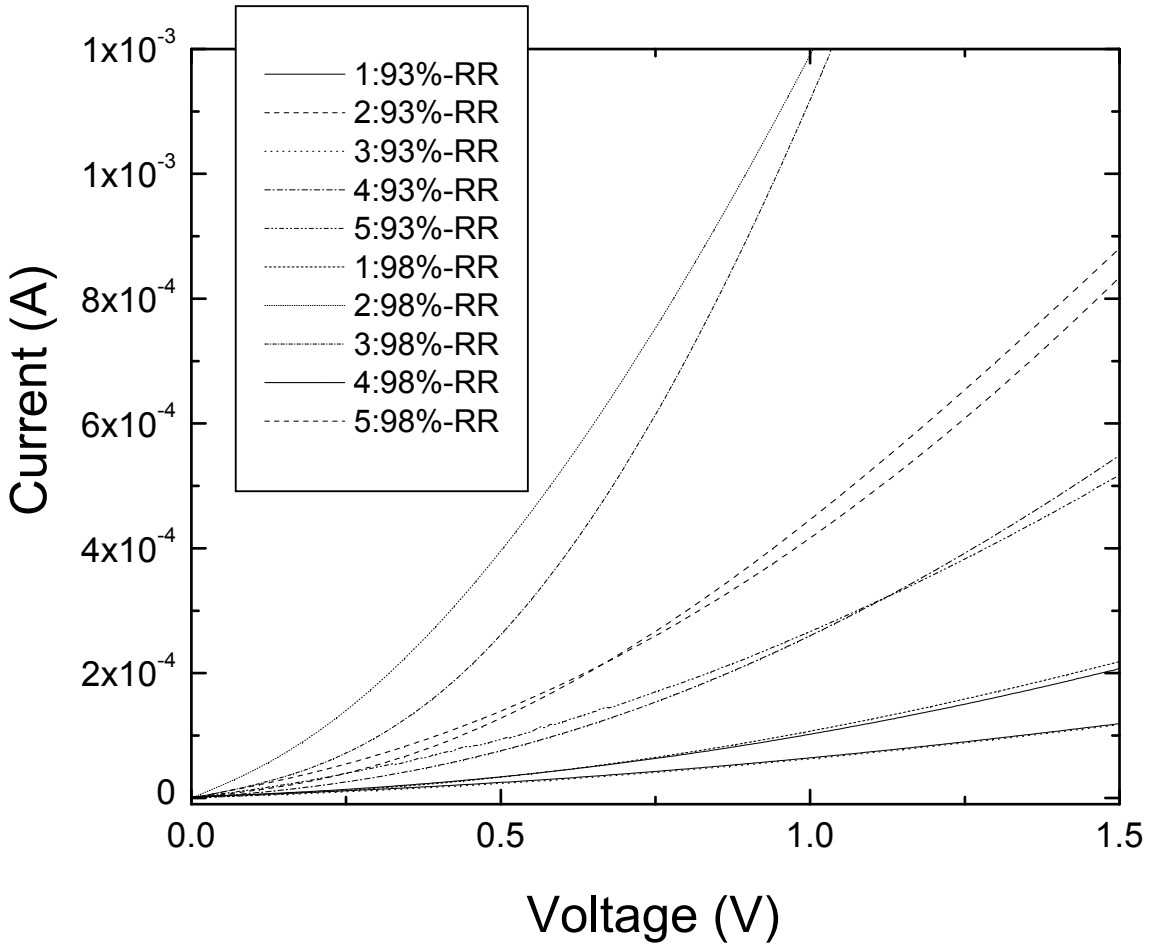

Figure D.2: Electron-only, 93% and 98%-RR dark current measurement of devices annealed 1 hour

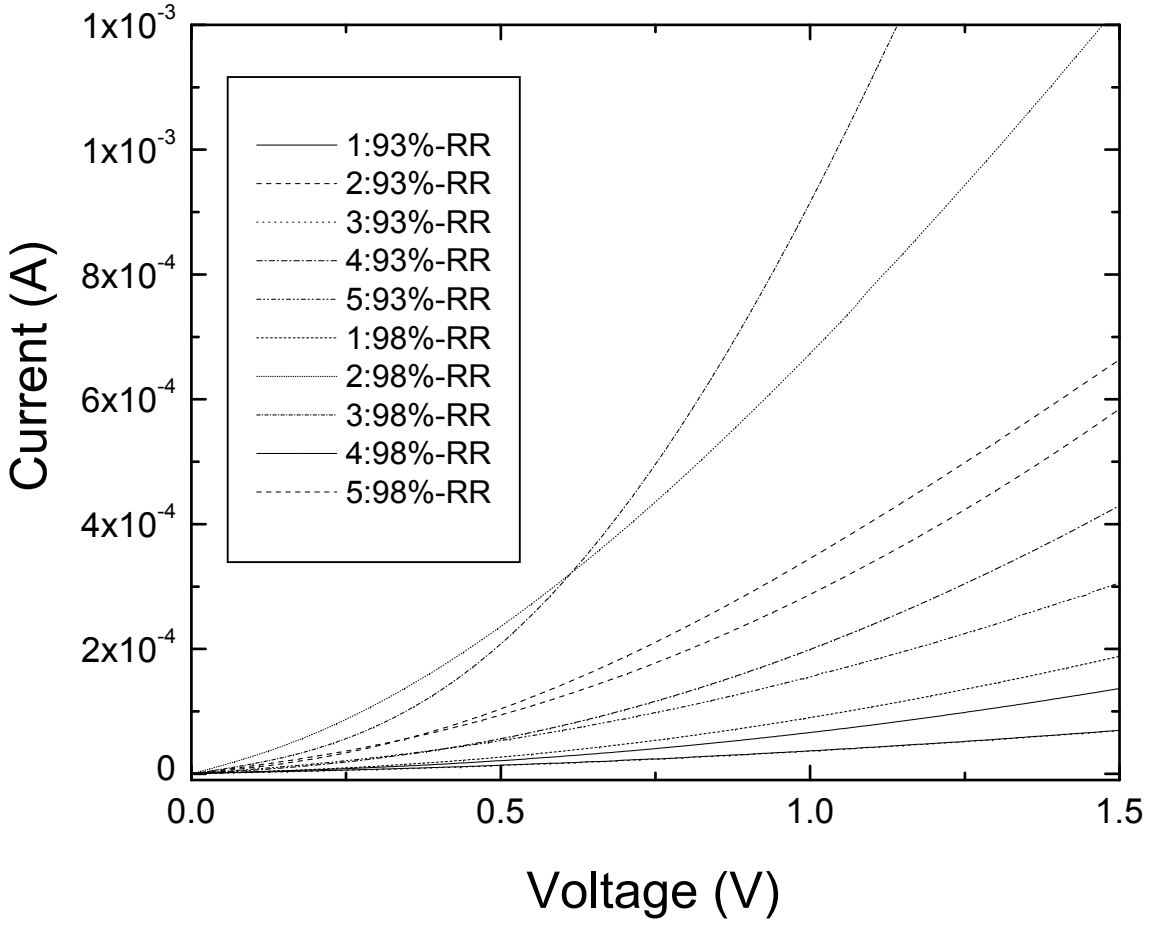

Figure D.3: Electron-only, 93% and 98%-RR dark current measurement of devices annealed 2 hours

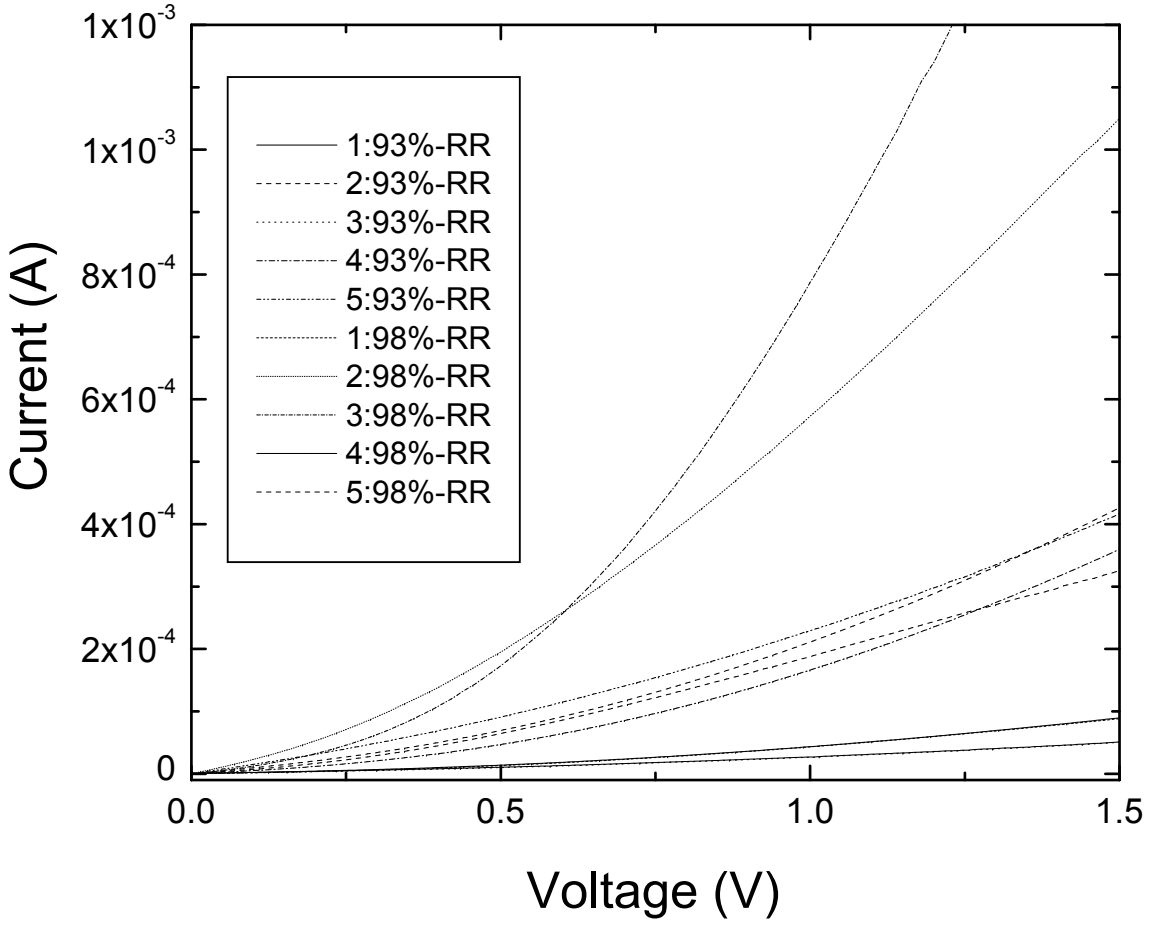

Figure D.4: Electron-only, 93% and 98%-RR dark current measurement of devices annealed 3 hours

Appendix E

$I - V$ for As-cast and Annealed 0%, 5% and 10%-ZnO

The following figures show the I-V characteristics measured for devices containing 0%, 5% and 10%-ZnO, and are numbered from 1 - 6. Each figure shows the performance before annealing.

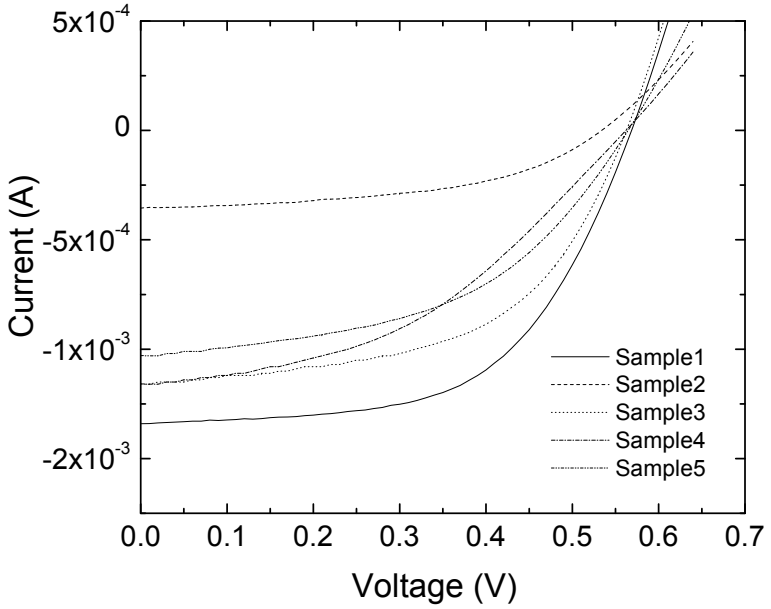

Figure E.1: $I - V$ for as-cast, 0%-ZnO devices

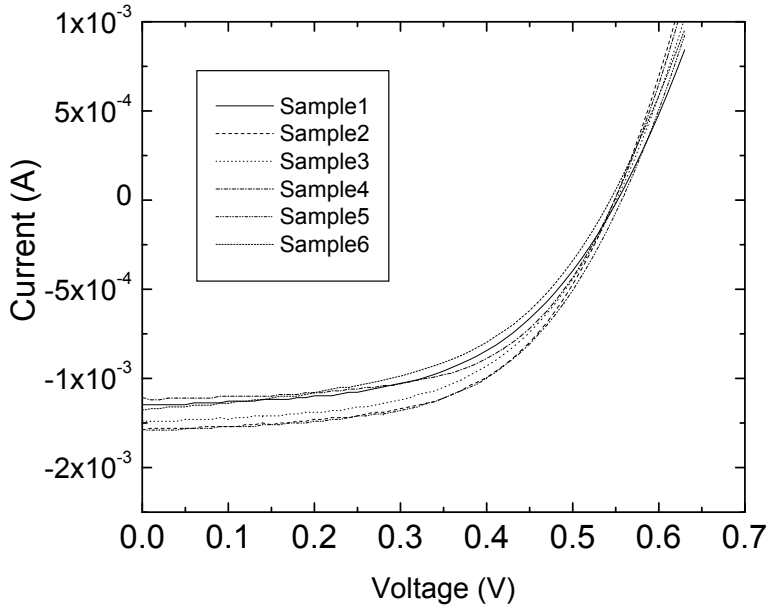

Figure E.2: $I-V$ for as-cast, 5%-ZnO devices

The following figures show the I-V characteristics measured for devices containing 0%, 5% and 10%-ZnO, and are numbered from 1 - 6. Each figure shows the performance after 1 hour of annealing.

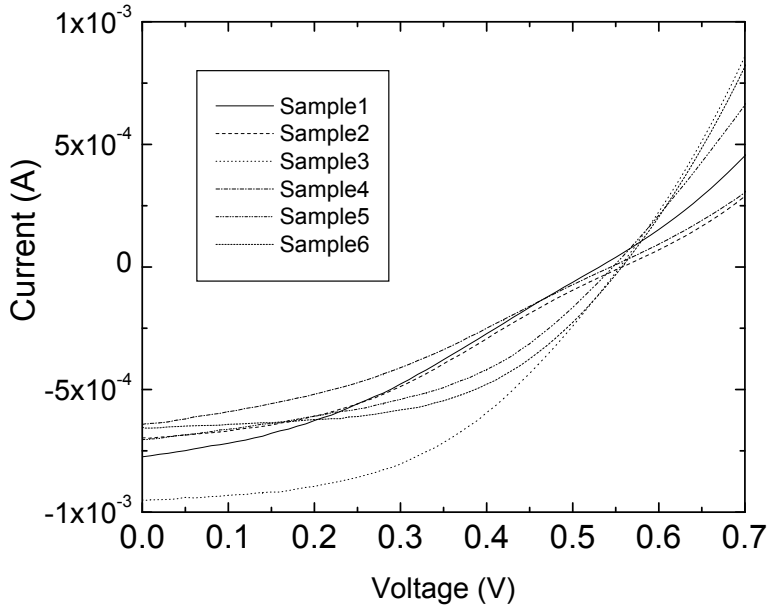

Figure E.3: $I - V$ for as-cast, 10%-ZnO devices

The following figures show the I-V characteristics measured for devices containing 0%, 5% and 10%-ZnO, and are numbered from 1 - 6. Each figure shows the performance after 2 hours of annealing.

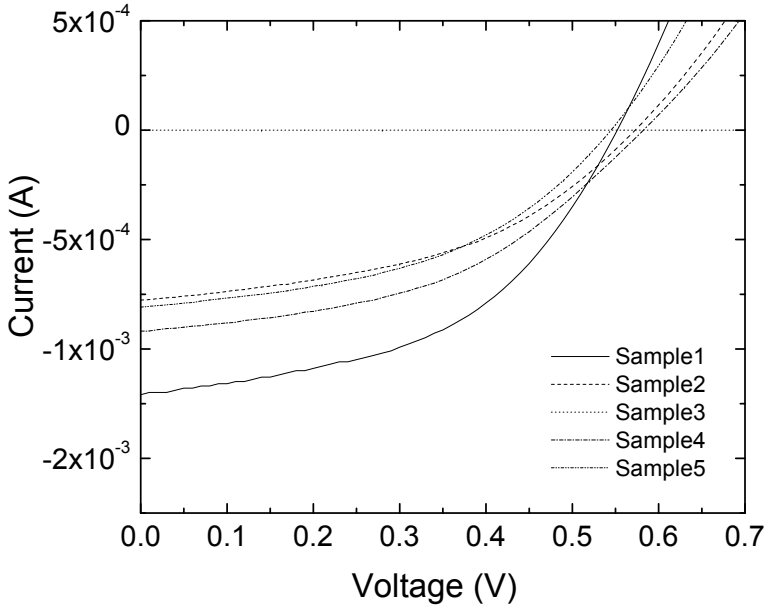

Figure E.4: $I - V$ for 0%-ZnO devices, annealed for 1 hour

The following figures show the I-V characteristics measured for devices containing 0%, 5% and 10%-ZnO, and are numbered from 1 - 6. Each figure shows the performance after 3 hours of annealing.

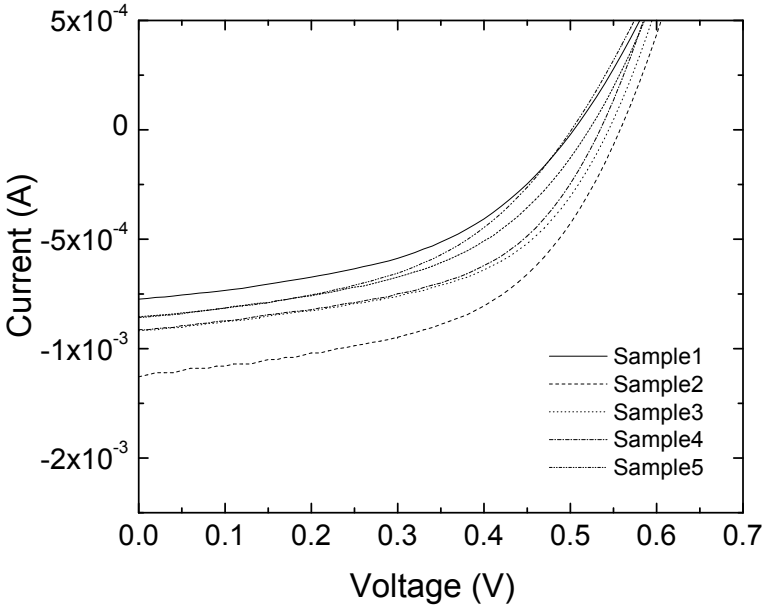

Figure E.5: $I-V$ for 5%-ZnO devices, annealed for 1 hour

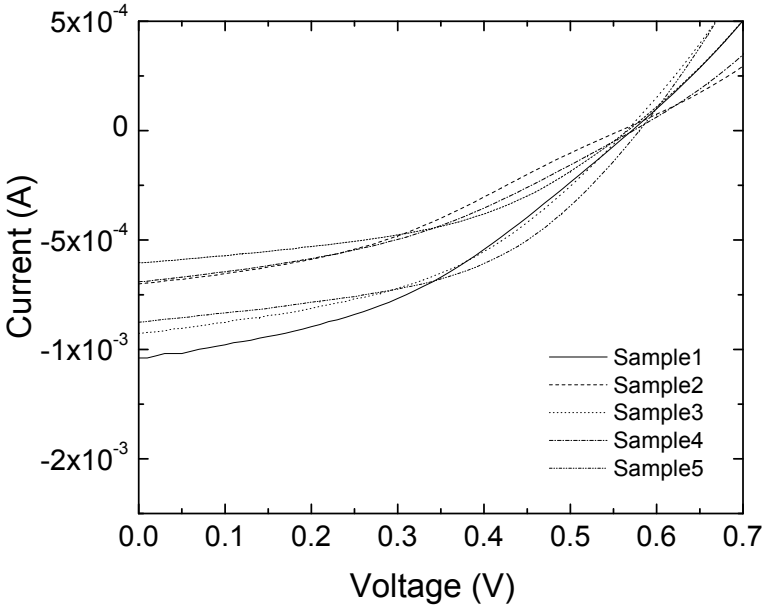

Figure E.6: $I-V$ for 10%-ZnO devices, annealed for 1 hour

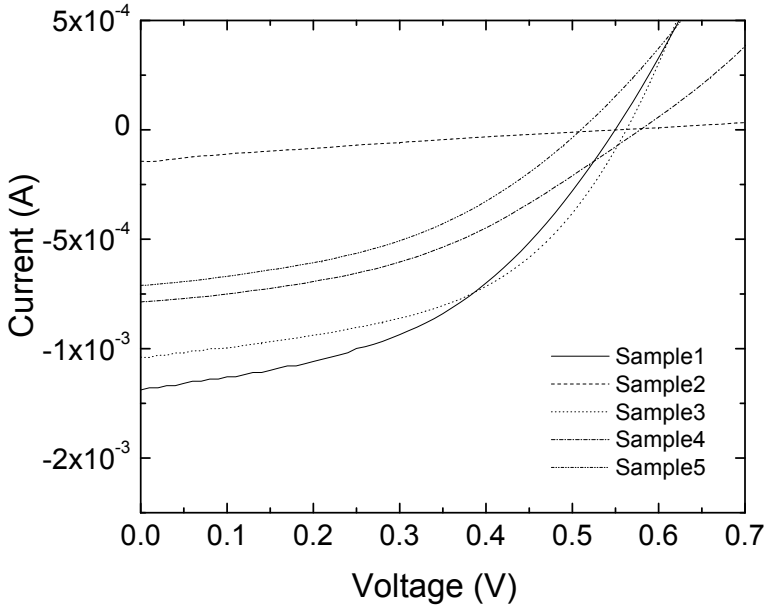

Figure E.7: $I-V$ for 0%-ZnO devices, annealed for 2 hours

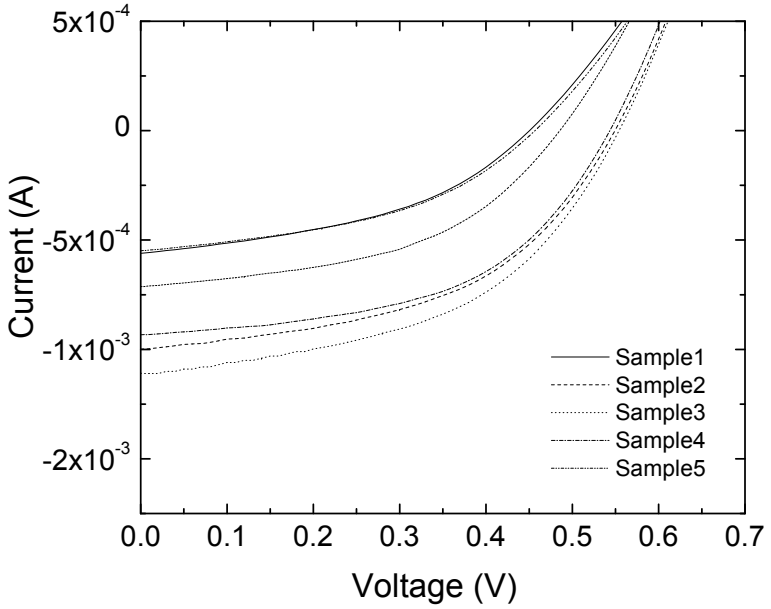

Figure E.8: $I-V$ for 5%-ZnO devices, annealed for 2 hours

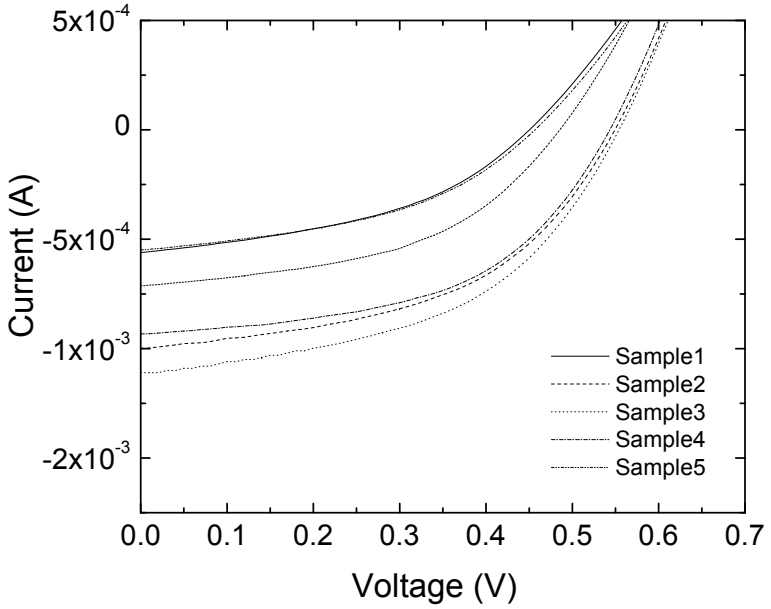

Figure E.9: $I-V$ for 10%-ZnO devices, annealed for 2 hours

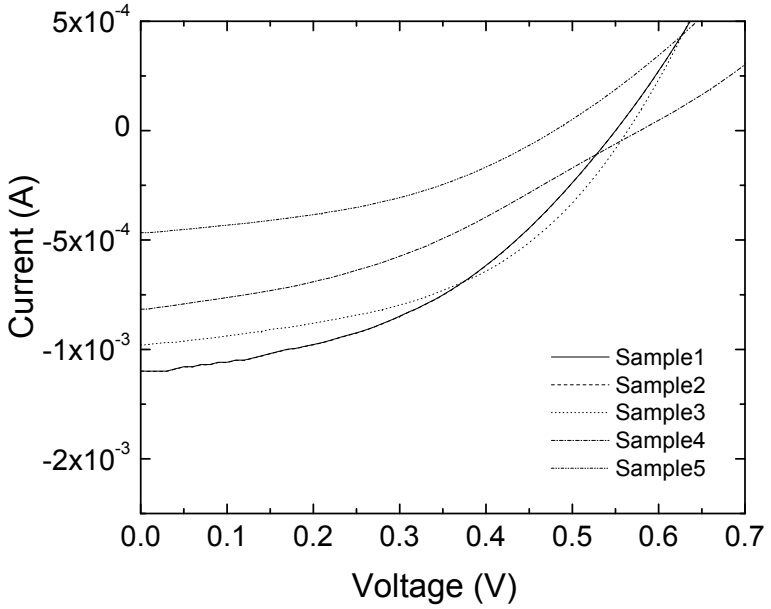

Figure E.10: $I-V$ for 0%-ZnO devices, annealed for 3 hours

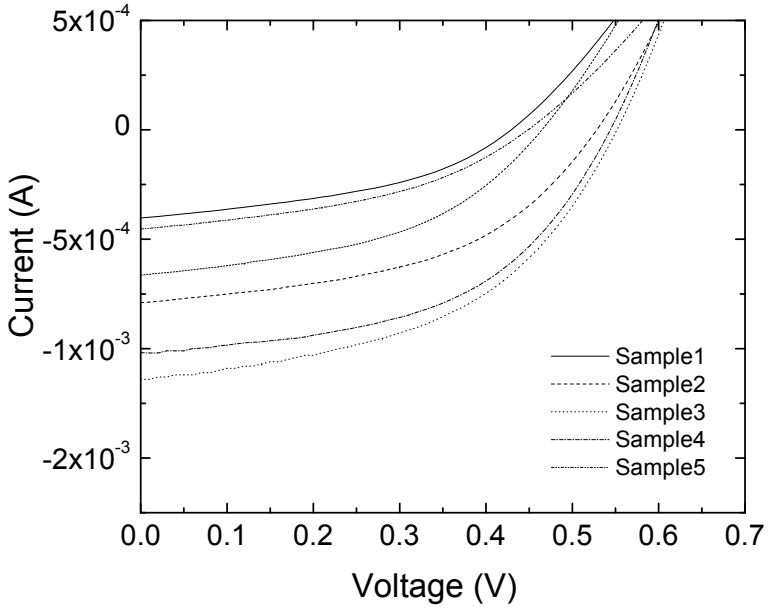

Figure E.11: $I-V$ for 5%-ZnO devices, annealed for 3 hours

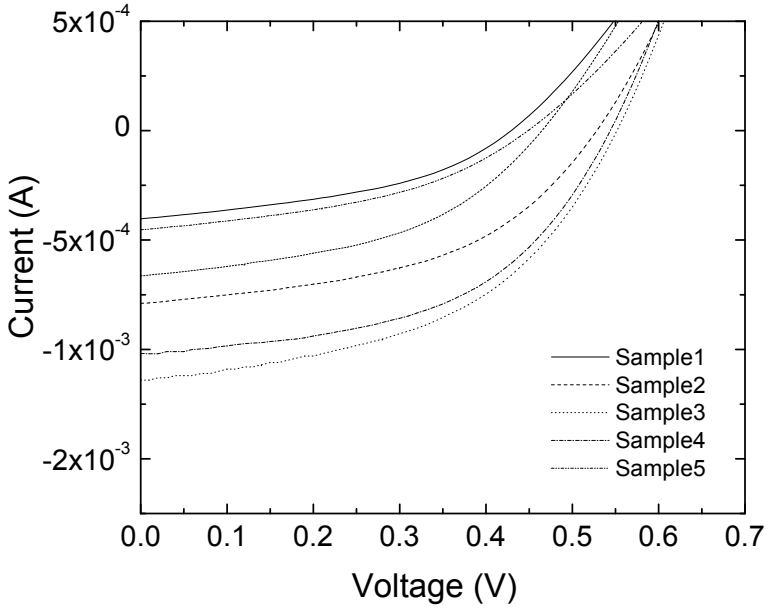

Figure E.12: $I-V$ for 10%-ZnO devices, annealed for 3 hours

Appendix F

UV-VIS for As-cast and Annealed Devices

The following figures show the results for the UV-VIS for 0%, 5% and 10%-ZnO devices, before and after annealing.

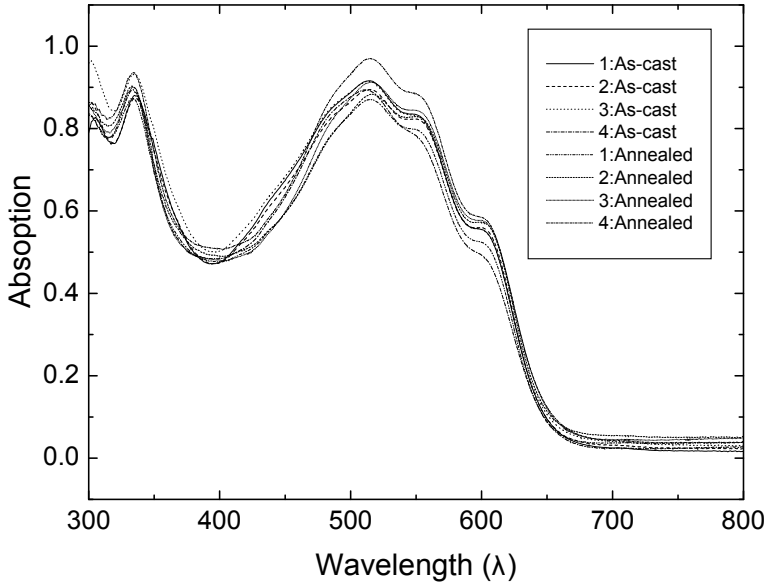

Figure F.1: UV-VIS for of 0%-ZnO devices, before and after annealing

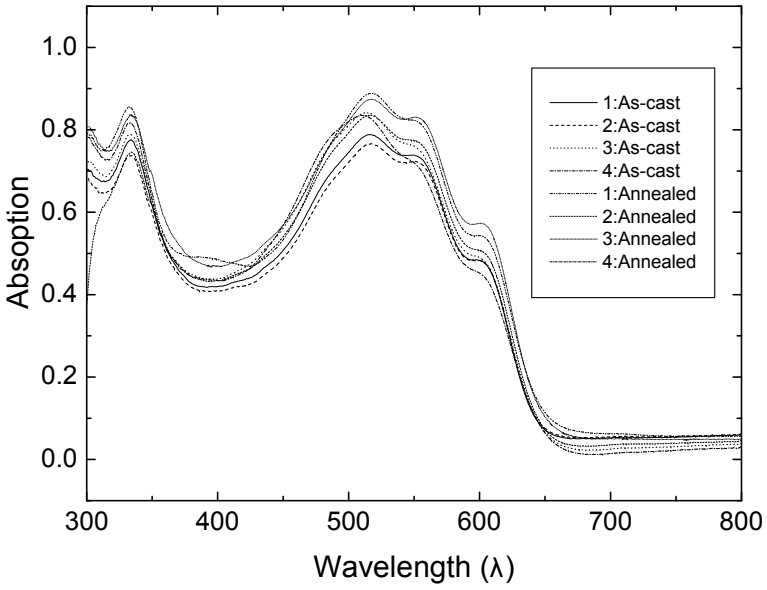

Figure F.2: UV-VIS for of low-ZnO devices, before and after annealing

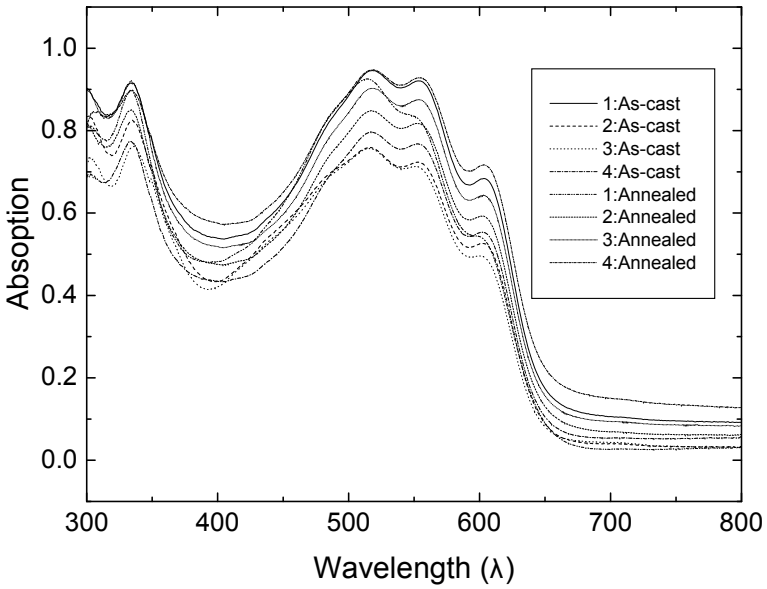

Figure F.3: UV-VIS for of high-ZnO devices, before and after annealing

Appendix G

Electron-only Dark Currents for 0%, 5% and 10%-ZnO Devices

The following figures show the results for electron only dark I-V measurements of all samples, numbered from 1-6, for devices containing 0%, 5% and 10%-ZnO. The first figure shows the measurements for devices before annealing, and the second and third figures show the measurements after 1 and 2 hours of annealing, respectively.

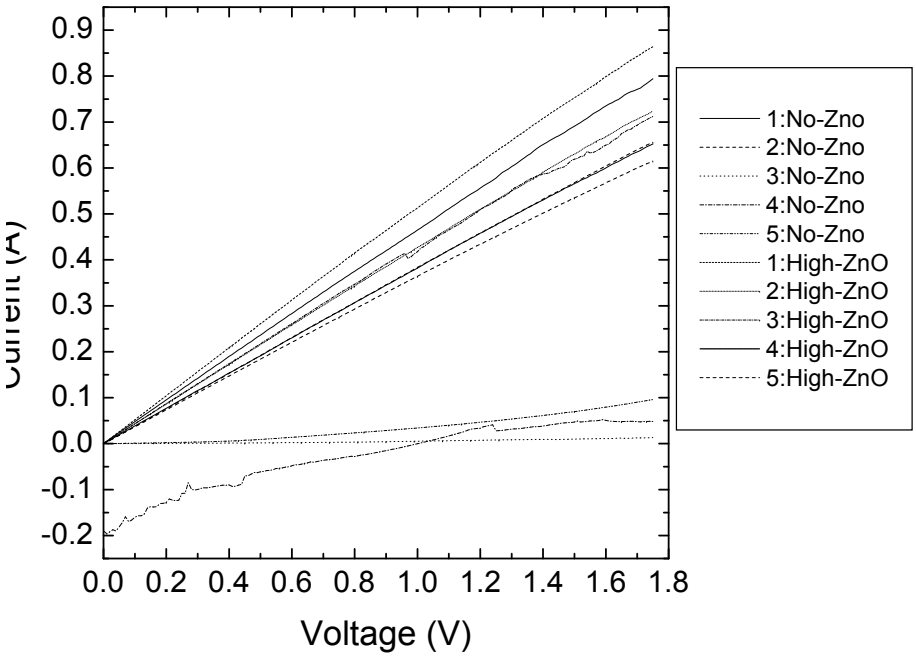

Figure G.1: Electron-only dark currents for as-cast devices

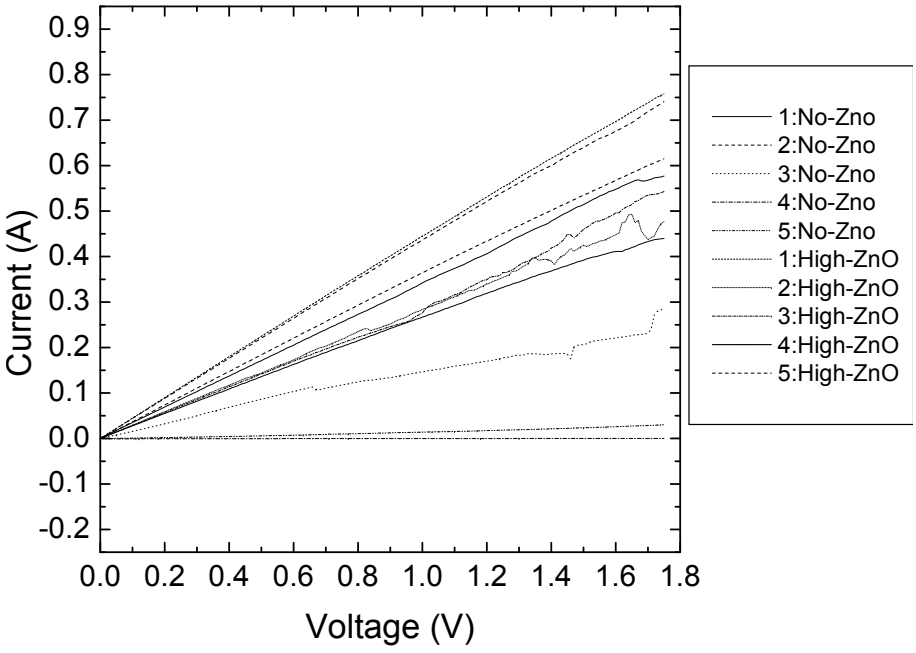

Figure G.2: Electron-only dark currents for devices annealed for 1 hour

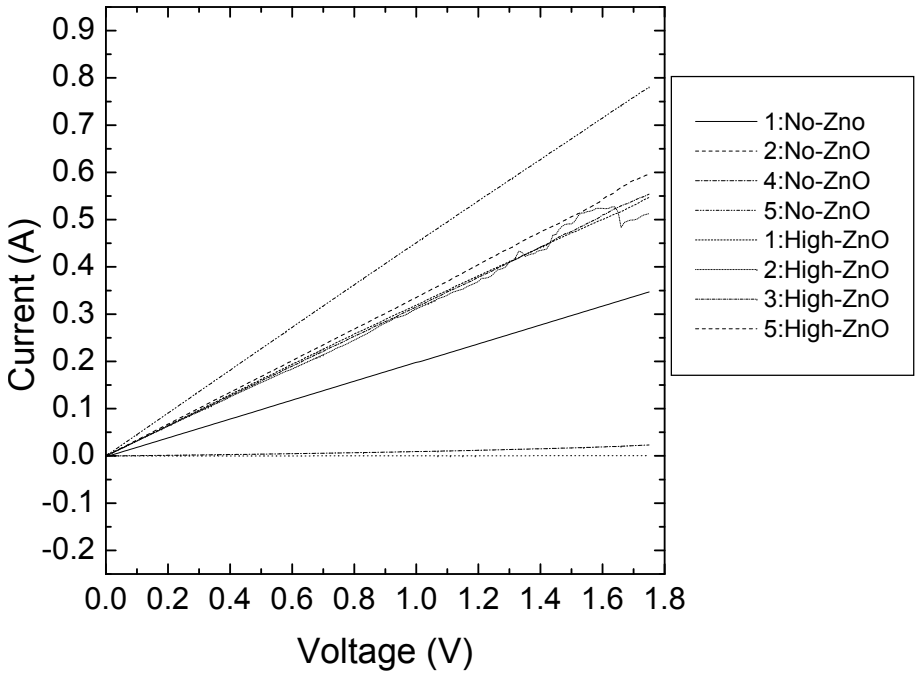

Figure G.3: Electron-only dark currents for devices annealed for 2 hours

Appendix H

Hole-only Dark Currents for 0%, 5% and 10%-ZnO Devices

The following figures show the results for hole only dark I-V measurements for all samples, numbered from 1-6, for devices containing 0%, 5% and 10%-ZnO. The first figure shows the measurements for devices before annealing, and the second and third figures show the measurements after 1 and 2 hours of annealing, respectively.

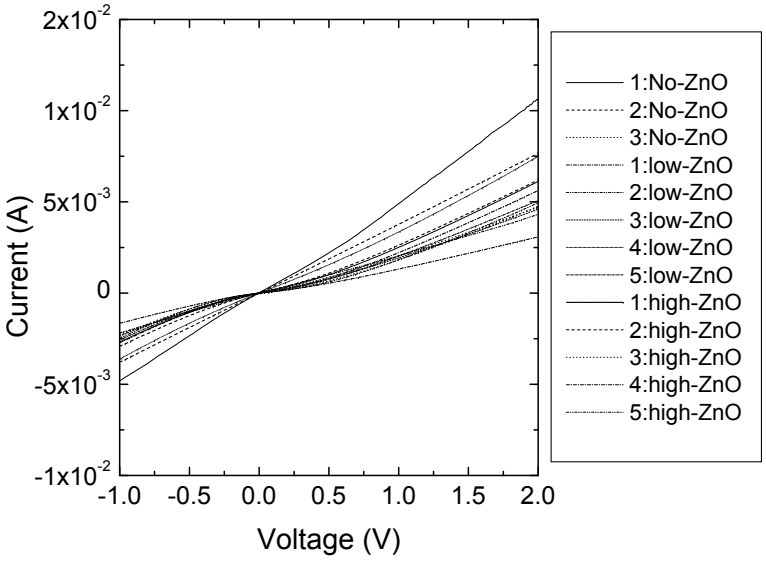

Figure H.1: Hole-only dark currents of as-cast devices

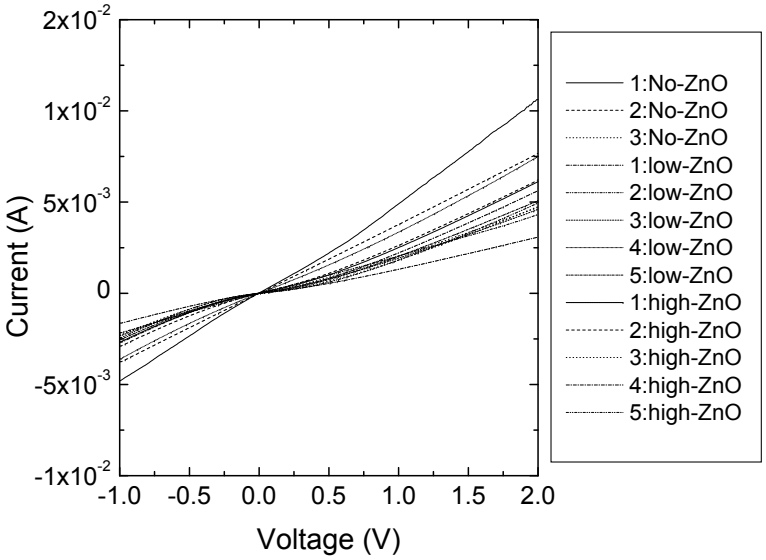

Figure H.2: Hole-only dark currents of devices annealed for 1 hour

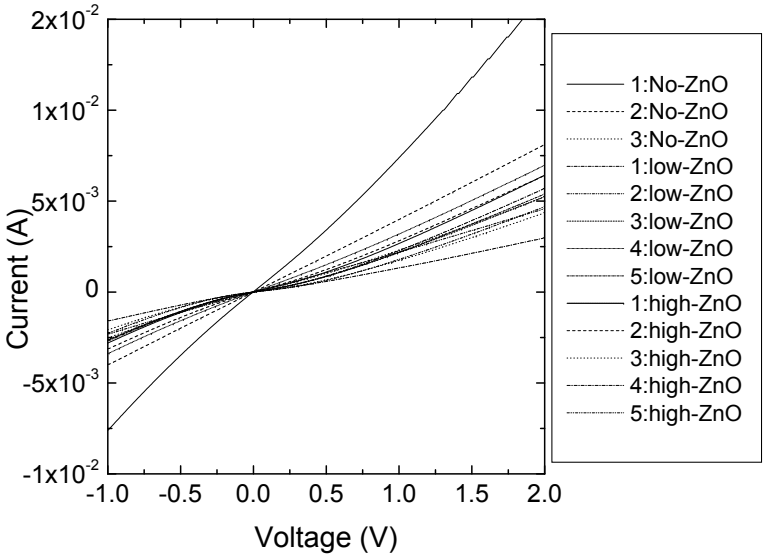

Figure H.3: Hole-only dark currents of devices annealed for 2 hours

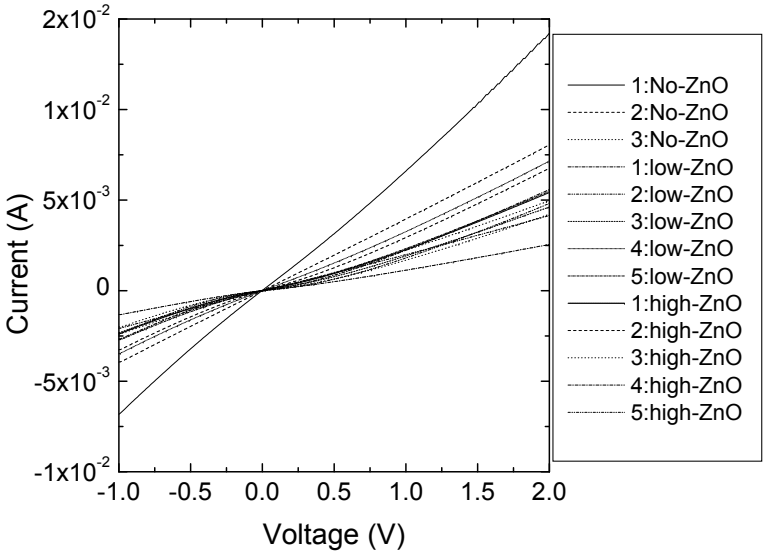

Figure H.4: Hole-only dark currents of devices annealed for 3 hours